International Journal of Heat and Fluid Flow 29 (2008) 1240–1257

Contents lists available at ScienceDirect

International Journal of Heat and Fluid Flow

journal homepage: www.elsevier.com/locate/ijhff

Turbulent heat and mass transfer in sinusoidal wavy channels

M.V. Pham, F. Plourde *, S.K. Doan

LET-ENSMA, UMR CNRS 6608, 1, Avenue Clément Ader, BP 40109, 86961 Chasseneuil Futuroscope Cedex, France

ARTICLE INFO

Article history:
Received 5 September 2007
Received in revised form 25 January 2008
Accepted 1 April 2008
Available online 18 July 2008

Keywords:
LES
Heat transfer
Wavy channel

ABSTRACT

Large-eddy simulation (LES) with dynamic modelling is used to investigate three-dimensional turbulent flow in wavy channels. An immersed numerical boundary technique on staggered Cartesian mesh grid simulates the complex geometry. Heat transfer is also placed into focus, while the numerical formulation is based on a low-Mach number weakly compressible formulation. For a given wavy channel geometry and considering several wavy periods, influence of *Re* Reynolds numbers ranging from 750 to 4500 allows an observer to clearly depict steady, unsteady and turbulent flow development. Identification of coherent structures sheds light on unstable vortex growth mechanisms, which favour the development of lateral fluctuation activity. The Fanning and Colburn coefficients are likewise presented and highly satisfactory agreement with available experimental data validates the numerical model employed. Finally, the effect of the ε spacing ratio is analyzed, and the results clearly show that small ε levels inhibit unstable mechanisms. At the same time, turbulent kinetic energy balance showcases the fact that the smaller ε, the more homogeneously turbulence behaves. Global heat and mass transfer underlines the direct role of ε in the control of overall heat transfer efficiency.

1. Introduction

Enhancement of heat and mass transfer is a major concern that is intimately linked to design optimization in heat-exchangers. As regards heat transfer, one way to increase it is provided by extended surfaces or fins in a variety of geometries such as offset-strip fins, louvered fins and corrugated or wavy fins among other. Even though efficiency in heat transfer is not at its highest in comparison with other geometries of similar cross-section, wavy channels are found to be attractive because they provide reduced pressure drop enabling them to offer superior thermal-hydraulic performance. In addition, as underlined by Manglik et al. (2005) their simplicity of manufacture renders such geometries attractive, and it surely explains recent interest in their flow field characterization. The geometrical characteristics of wavy channels consist in their sinusoidal shape described by *A* amplitude, *L* wavelength or pitch of waviness, *H* fin height and *S* fin spacing. Experimenters generally introduce the three dimensionless parameters representing the geometry: channel spacing ratio ($\varepsilon = S/2A$), flow cross-section ($\alpha = S/H$) and waviness aspect ratio ($\gamma = 2A/L$). Up until now, most of their studies on heat and mass transfer in wavy-plate-fins have focused on the effects of the geometry by modifying ε, α and γ as well as the flow rate on overall heat and mass transfer. For instance, Zhang et al. (2004) have investigated laminar forced convection in two-dimensional sinusoidal channels for wall-corrugation severity ($0.125 \leqslant \gamma \leqslant 0.5$) and fin spacing ($0.1 \leqslant \varepsilon \leqslant 3.0$) with Reynolds numbers generally lower than $Re = 1000$. The sensitive influence of the flow geometry on local velocity and temperature distribution was clearly demonstrated, as was the nature of wavy surface-induced lateral vortex structure, in the framework of evaluation of enhanced thermal-hydraulic performance. Under the chosen range of Reynolds numbers, wall-curvature induces fluid separation downstream from the wavy surface peak that provides a recirculation cell in the wall-valley regions. The latter was found to grow in magnitude, and spatial flow converges with increasing *Re* and/or γ. In addition, inter-plate separation has likewise been found to be a critical parameter as well; viscous forces dominate with small separation while for large inter-plate separation, it gives rise to a vortex flow structure in the valley region. Several investigations have numerically addressed the issue of forced convective heat and mass transfer in wavy channels but only a few have provided comparisons of experimental and numerical data. Taking into account the sizes of the wavy channel in compact heat-exchangers, experiments have generally been focused on the overall heat and pressure drop; recently, Zhang et al. (2003) compared their numerical predictions of the *f* Fanning friction factor and *j* Colburn factor with experimental investigations in the range of $10 \leqslant Re \leqslant 1500$ and according to the authors, the numerical and experimental data are in excellent agreement. In their study, numerical simulations were carried out for two sinusoidal geometries in the given Reynolds number range while experimental tests were performed for similar geometries in a wider Reynolds range ($Re \leqslant 7000$). For either *j* or *f* in the common

* Corresponding author. Tel.: +33 549498119; fax: +33 549498130.
E-mail address: plourde@let.ensma.fr (F. Plourde).

0142-727X/$ - see front matter © 2008 Elsevier Inc. All rights reserved.
doi:10.1016/j.ijheatfluidflow.2008.04.002

Nomenclature

A	wavy amplitude (m)
C_s	Smagorinsky coefficient
C_d	dynamic coefficient
c_p	specific heat (J/kg K)
D_h	hydraulic diameter (=2S)
H	fin height (m)
h_j	subgrid scale heat flux
I_T	thermal turbulent intensity
I_u	dynamic turbulent intensity
L	wavelength (m)
k_0	thermal conductivity of the fluid at inlet condition (W/m K)
$L_x \times L_y \times L_z$	computational domain length in x-, y-, z-direction, respectively, normalized by L
S	fin spacing (m)
s_{ij}	rate of strain tensor
t	normalized time
T	temperature (K)
u, v, w	velocity components normalized by U_0
U_0	inlet reference velocity (m/s)
u_τ	friction velocity normalized by U_0
x, y, z	non-dimensional co-ordinate normalized by L

Greek symbols

Δ	characteristic grid spacing (=$(\Delta x \Delta y \Delta z)^{1/3}$)
Δx, Δy, Δz	grid spacing in x-, y-, z-directions
λ	non-dimensional wavelength normalized by L
λ_{ci}	imaginary part of velocity gradient tensor complex eigenvalue
τ_{ij}	subgrid scale tensor
τ_w	wall shear stress
ρ_0	density at inlet condition (kg/m^3)
ρ	fluid density normalized by ρ_0
θ	normalized temperature (=$(T - T_w)/(T_0 - T_w)$)
μ_0	dynamic viscosity (kg/m s)
μ_l	dynamic viscosity normalized by μ_0
μ_t	turbulent dynamic viscosity normalized by μ_0

Dimensionless parameters

α	flow cross-section parameter (=S/H)
ε	spacing ratio (=$S/2A$)
γ	waviness parameter (=$2A/L$)
f	Fanning friction factor
j	Colburn factor (=$Nu/RePr^{1/3}$)
Nu	Nusselt number
Pr	Prandtl number (=$\mu_0 c_p/k_0$)
Pr_t	turbulent Prandtl number
Re	Reynolds number (=$\rho_0 U_0 D_h/\mu_0$)

Subscripts

0	inlet condition
w	referred to wall condition

Superscripts

$\bar{}$	large-scale component of filtered quantity
$\wedge$	test filtering with double width filter wider than grid filter width
$\sim$	large-scale component of Favre filtered quantity
$\langle\,\rangle$	spatial averaging operator

Reynolds range, the numerical predictions fall within ±8% of the experimental data and according to Zhang et al. (2003), this amply validates the numerical modelling and simulation. In addition, the extrapolated trend of numerical predictions pretty much agrees more or less with the experimental data. One should nonetheless underline that under such a wide range of Reynolds number, effects of turbulence may impact heat and mass transfers. The use of large-eddy simulations and to some extent direct simulations is becoming increasingly common in model complex flow geometries. One of the earliest applications to go beyond the horizontally homogeneous channel case involved modelling turbulence convective flow over wavy terrain, i.e. over a sinusoidal surface. This research effort was oriented mainly towards atmospheric flows, and several turbulent simulations addressing the point may be found in the literature. Direct simulations of channel flow over wavy surface (Cherukat et al., 1998; De Angelis et al., 1997) have successfully reproduced many of the laboratory observations for moderate Reynolds numbers while also providing comprehensive details on the flow structure. De Angelis et al. (1997) established a turbulent energy budget from direct simulations that entail a redistribution of energy moving from streamwise to spanwise and wall-normal directions; the transfer takes place in a thin layer close to the boundary downstream from wave troughs. The effect becomes more pronounced when the amplitude increases and energy is redistributed primarily into spanwise fluctuations. Henn and Sykes (1999) proposed detailed comparisons between experimental and numerical results obtained from large-eddy simulation; they also underlined a significant increase of spanwise fluctuations on the wave up-slope that is linked to temporally persistent vortex-like structures localized near the surface. Calhoun and Street (2001) analyzed turbulent flow over a wavy surface and from a vortex identification method streamwise vortices were found to be locked into a phase relationship with the wavy boundary. Thus, these vortices may be linked to the Görtler instability mechanism caused by the wavy wall. Tseng and Ferziger (2004) have recently followed the development of these Görtler vortices by using an efficient immersed boundary method to simulate turbulent flow over a wavy channel. Large-eddy simulation facilitates depiction of vortices and, more specifically, of Görtler structures that are formed by a sequential vortex reconnection process and broken down on account of vortex separation. According to Saric and Benmalek (1991), the spatial evolution of Görtler vortex involves not only a single instability mechanism but also secondary instability, initial condition, local topography effect, open convective flow, etc. These interactions cannot be addressed correctly by the local analysis and linear stability theory. Thus, the formation of Görtler vortices significantly depends on the stabilization/destabilization effects on the convex/concave portion of the wavy surface. To authors' knowledge, the convective instability that develops in a sinusoidal channel has not yet been addressed except as regards a symmetric sinusoidal channel (Blancher et al., 1998; Blancher et al., 2004). Results clearly showed that unsteady fully developed flow in periodic section geometry needs to be carried out in domains consisting of several periodicity lengths differing from what is generally done. Nishimura and Matsume (1998) conducted experiments and numerical analysis to study the effect of frequency of fluid oscillation on the dynamical behaviour of vortices on two different wavy walled channels for pulsatile flow. They clearly demonstrated that an optimum frequency produces optimal heat and mass transfer ratio at low Reynolds numbers. Considering heat and mass transfer, it is helpful to quote Choi and Suzuki (2005), who investigated from LES numerical investigation turbu-

lent flows; they studied heat transfer in a channel with only one wavy wall and paid specific attention to the effect of the near-wall streamwise vortices on the turbulent thermal fields. Niceno and Nobile (2001) conducted numerical analysis that clearly highlighted the fact that wavy channels are effective geometries enhancing heat transfer in unsteady regimes.

Our research provides a complementary outlook on the flow field that develops in a wavy channel. We initially decided to address heat and mass transfer efficiency for a wide range of Reynolds numbers ($750 \leqslant Re \leqslant 4500$) in order to shed light on the flow field behaviour that develops under turbulent regime. To depict transition process from laminar to turbulence, several sinusoidal wavy periods have been taken into account. A quantitative validation proved necessary and was carried out as in Zhang et al. (2003), i.e. by comparing numerical predictions of j and f coefficients with available experimental results. One key point of our analysis is to identify structures and to discuss the influence of a sinusoidal top wall presence on turbulent transfers; in fact, as underlined above, there have been many studies dedicated to turbulence analysis of a free flow over a wavy surface but not nearly as many in a wavy channel. Influence of channel spacing, i.e. influence of ε channel spacing ratio, is also considered for a turbulent flow field regime.

2. Numerical method and model description

2.1. Governing equations and large-eddy simulation

In large-eddy simulation, each variable f is split into a large anisotropic scale $\tilde{f}$, which is computed, and a small-scale component $\tilde{f}'$. In order to take into account the change of density, a density-weighted Favre average is applied as $\tilde{f} = \widetilde{\rho f}/\bar{\rho}$. The flow is governed by the three-dimensional time-dependent Navier–Stokes equations for a low-Mach number weakly compressible formulation:

$$\frac{\partial \bar{\rho}}{\partial t} + \frac{\partial}{\partial x_j}(\bar{\rho}\tilde{u}_j) = 0 \tag{1}$$

$$\frac{\partial \tilde{u}_i}{\partial t} + \tilde{u}_j \frac{\partial \tilde{u}_i}{\partial x_j} = -\frac{\partial \bar{p}}{\bar{\rho}\partial x_i} + \frac{1}{\bar{\rho} Re}\frac{\partial \tilde{\tau}_{ij}}{\partial x_j} + F_i \tag{2}$$

$$\frac{\partial \tilde{\theta}}{\partial t} + \tilde{u}_j \frac{\partial \tilde{\theta}}{\partial x_j} = \frac{\partial \tilde{h}_j}{\bar{\rho}\partial x_j} + \Phi \tag{3}$$

where all the variables are non-dimensionalized by a characteristic distance representing the wavelength (L), inlet characteristic velocity (U_0) and inlet dynamic pressure ($\rho_0 U_0^2$). F_i and Φ are, respectively, momentum and energy term sources and would be defined hereinafter (see Eqs. (11) and (12)). Normalized temperature θ is equal to $\theta = \frac{T - T_w}{T_0 - T_w}$, where T_0 denotes the inlet temperature of fluid and is set equal to 373 K while T_w the fin wall temperature is equal to 293 K. The reference thermodynamic and transport properties of the fluid, such as reference density (ρ_0), viscosity (μ_0) and conductivity (k_0), are also assumed to remain at a constant level and are evaluated at inlet conditions.

In this low-Mach number formulation, acoustic wave propagation is ignored and pressure field correspond to a hydrodynamic component $\check{p}(\mathbf{x}, t)$. Fluid density is derived from the ideal gas equation state. The dimensionless parameters are the Reynolds and Prandtl numbers, which are defined as $Re = \rho_0 U_0 D_h/\mu_0$ and $Pr = \mu_0 c_p/k_0$, where c_p is the specific heat of the fluid and D_h is the hydraulic diameter. Under the range of temperatures studied, one may consider the Prandtl number as a constant equal to 0.71 corresponding to that of air while inlet velocity magnitude is considered as a variable so as to regulate the Re Reynolds number from 750 to 4500. However, dependency of the molecular viscosity and temperature was taken into account by the Sutherland law. The total stresses are $\tilde{\tau}_{ij} = 2(\mu_l + Re\,\mu_t)\tilde{s}_{ij}$, where the $\tilde{s}_{ij}$ strain-rate tensor is:

$$\tilde{s}_{ij} = \frac{1}{2}\left(\frac{\partial \tilde{u}_i}{\partial x_j} + \frac{\partial \tilde{u}_j}{\partial x_i}\right) - \frac{1}{3}\delta_{ij}\frac{\partial \tilde{u}_k}{\partial x_k} \tag{4}$$

Similarly, the total heat flux may be written as

$$\tilde{h}_j = \left(\frac{1}{Re}\frac{\mu_l}{Pr} + \frac{\mu_t}{Pr_t}\right)\frac{\partial \tilde{\theta}}{\partial x_j} \tag{5}$$

In this LES formulation, the subgrid scale viscosity is correlated with the deformation of the resolved velocity field as

$$\mu_t = \bar{\rho}(C_s \Delta)^2 |\tilde{s}| = \bar{\rho}(C_s \Delta)^2 (2\tilde{s}_{ij}\tilde{s}_{ij})^{1/2} \tag{6}$$

with $\Delta = (\Delta x \Delta y \Delta z)^{1/3}$. In the present study, the Smagorinsky coefficient $C_s = \sqrt{C_d}$, which was estimated through a dynamic model (Germano et al., 1991), is time and space-dependent. To do so, another filtering procedure is introduced and is mathematically represented by a hat ($\hat{f}$). After which, an accurate calculable relationship between the subgrid scale stress tensors at the two different filter widths enables an observer one to dynamically estimate the Smagorinsky coefficient:

$$C_s = \sqrt{C_d} \quad \text{with} \quad C_d = -\frac{L_{ij}^d M_{ij}}{M_{ij} M_{ij}} \tag{7}$$

where the second-order tensors L_{ij} and M_{ij} are given as follows:

$$\left.\begin{aligned} L_{ij} &= \bar{\rho}\widehat{\tilde{u}_i \tilde{u}_j} - \hat{\bar{\rho}}\hat{\tilde{u}}_i \hat{\tilde{u}}_j \\ M_{ij} &= (\alpha_{ij} - \hat{\beta}_{ij}) \end{aligned}\right\} \tag{8}$$

with: $\beta_{ij} = 2\bar{\rho}\Delta^2|\tilde{s}|\tilde{s}_{ij}$, $\alpha_{ij} = 2\hat{\bar{\rho}}\hat{\Delta}^2|\hat{\tilde{s}}|\hat{\tilde{s}}_{ij}$ and $L_{ij}^d = L_{ij} - \frac{1}{3}\delta_{ij}L_{kk} = -C_d\alpha_{ij} + \widehat{C_d\beta_{ij}}$.

However, the mathematical procedures to determine C_d may generate non-physical values (zero even negative) in areas such as wall vicinity and laminar/turbulent transition. These negative values may introduce undesirable numerical instabilities. In order to enhance the numerical stability of the model, attention must be paid to some specific points. One should first use the averaged C_d in a direction homogeneous to the flow (Germano et al., 1991) when the latter is clearly identified. However, it is easier to limit the C_d level to a predetermined range (Zang et al., 1993). Actually, in complex geometries such as the one studied, no homogeneous directions are enhanced and it is preferable to bound the dynamic coefficient (Conway et al., 2000). In the present simulation, C_s is clipped between 0 and 0.21. A posteriori check underlined than around 60% of C_s coefficient estimation fall within the prescribed range and Pham et al. (2008) recently emphasized that dynamic modelling improve overall friction estimation.

A similar approach was applied to estimate Pr_t turbulent Prandtl number. The thermal-dynamic coupling is taken into account throughout a similar dynamic procedure in order to estimate the Pr_t turbulent Prandtl number:

$$Pr_t(\mathbf{x}, t) = -C_d\frac{Q_j Q_j}{P_j Q_j} \tag{9}$$

$$\text{with } P_j = \widehat{\bar{\rho}\tilde{u}_j\tilde{\theta}} - \hat{\bar{\rho}}\hat{\tilde{u}}_j\hat{\tilde{\theta}} \text{ and } Q_j = 2\hat{\bar{\rho}}\hat{\Delta}^2|\hat{\tilde{s}}|\frac{\partial\hat{\tilde{\theta}}}{\partial x_j} - 2\bar{\rho}\Delta^2\widehat{|\tilde{s}|\frac{\partial\tilde{\theta}}{\partial x_j}} \tag{10}$$

The procedure for dynamically estimating Pr_t is similar to the one applied by Zhang and Chen (2000).

The governing equations are discretized on a staggered grid in Cartesian coordinates with a second-order accurate finite difference scheme in space. Time advancement is carried out using a Mac-Cormack scheme with predictor–corrector steps. A projection method (Najm et al., 1998) is used to decouple momentum,

continuity and energy equations, while the resulting Poisson equation for pressure is solved by spectral method in parallel multiprocessors (Pham et al., 2007). A more detailed description of the numerical procedure is given in Pham et al. (2003).

2.2. Treatment of boundary using immersed boundary method

In order to consider wavy walls, we have developed an immersed boundary technique similar to the one proposed by Yang and Balaras (2006). Their method is based mainly on a direct forcing point analysis. In fact, Eulerian grid on Cartesian coordinates is used for numerical simulations, and in order to represent the complex rigid boundary, a F_i forcing point term is implicitly added to the momentum equations implicitly through the forcing point cells (Balaras, 2004). In this case, forcing is considered in the framework of the discretized equations and is explicitly defined so as to enforce the appropriate boundary conditions. As a result, a complex domain such as wavy channels can be simulated through this technique on a Cartesian regular grid. Thus, F_i is correct when location of unknowns coincides with the immersed boundary, but this is rarely the case for complex geometries. In order to estimate the corresponding F_i forcing points as a general rule, several techniques exist, and they may be divided into two groups. In the first one forcing points are defined in the vicinity of the immersed boundary while the second is built around a local reconstruction of the solution based on the boundary value. In fact, the original Peskin's method (Peskin, 1972; Peskin, 1977) which substitutes a discrete Dirac δ function in Eq. (2) belongs to the first category. This first technique has been widely used in biomedical domain and found to be robust. Lai and Peskin (2000) developed it on formal second-order accuracy. On the other hand, local reconstruction schemes have been found to be more flexible (Fadlun et al., 2000; Udaykumar et al., 2001) and can ensure high degrees of accuracy. Several variations involving this technique have been recently and successfully carried out (Yang and Balaras, 2006; Tseng and Ferziger, 2003) while the highly popular reconstruction ghost-cell technique has been used for various geometries included flow over a wavy surface; comparisons with body-fitted technique emphasize the particularly high potential of immersed boundary methods. However, the ghost-cell method is not easy to develop when dealing with moving boundary problems. Yang and Balaras (2006) proposed a similar local reconstruction but instead of applying conditions on ghost-cells, they favoured direct enforcement on fluid flow points, and this technique was found to be more robust and accurate for a higher-order scheme. The present work is based on the latter when simulating turbulent and heat transfers occurring in a wavy channel. In fact, we have extended the Yang and Balaras method to tackle heat transfer and an energy equation has been introduced.

In order to simulate wavy wall channels, an immersed boundary technique with forcing point reconstruction was developed, and its main features are detailed hereinafter. First a Cartesian mesh was considered and mesh points split into three different categories: (a) forcing points, which correspond to fluid points that have at least one neighbouring point in the solid phase, (b) solid points and (c) the remaining points that correspond to fluid points (see Fig. 1a). Since we employed a staggered grid location, forcing points are found to be different for each velocity components and

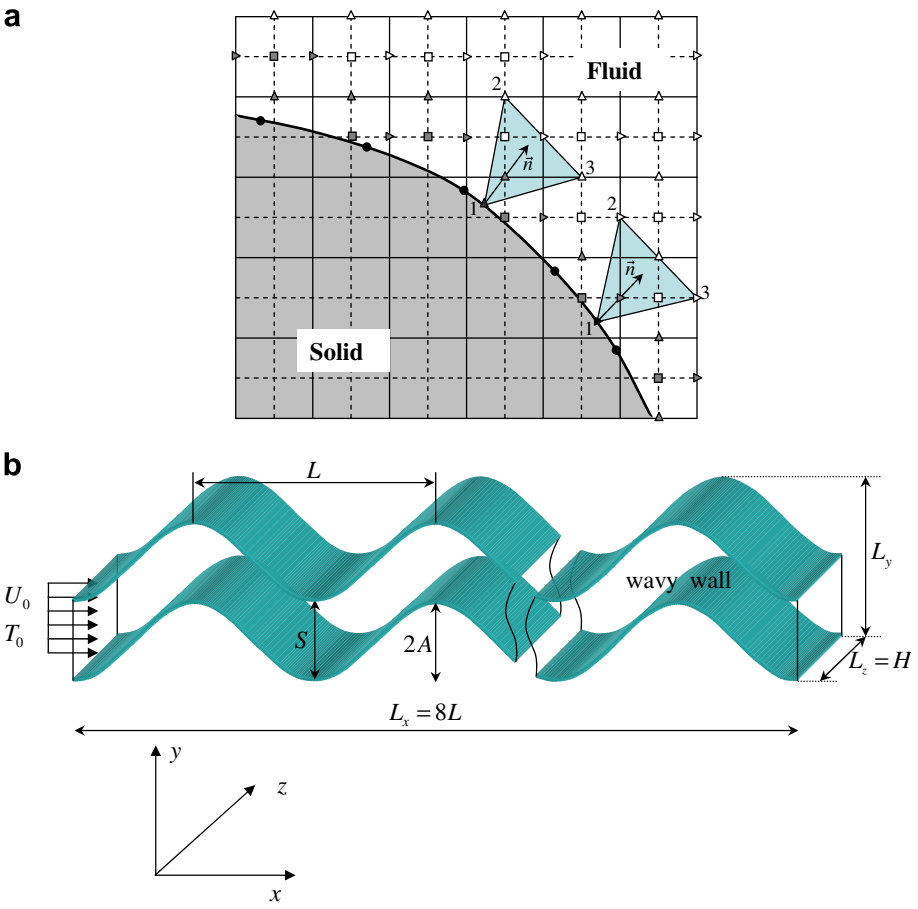

Fig. 1. (a) Example of 2D arrangement of flow variables on the staggered grid. (b) Schematic view of the computational domain: (▷) u, velocity; (△) v, velocity, (□) scalar nodes – filled symbols correspond to forcing points.

temperature. Considering the fact that wall temperature is assumed to remain at a constant level, Dirichlet conditions were applied on every forcing point, i.e. all along the immersed boundary interface that corresponds to the wavy wall. For instance, for the momentum equation, the magnitude of the forcing point F_i^k is enforced from Eq. (2) for each step in the predictor–corrector MacCormack scheme is:

$$F_i^k = \frac{u_s - \tilde{u}_i^k}{\Delta t} - \mathrm{RHS}_i^k \tag{11}$$

where RHS_i^k contains convective, viscous and pressure gradient terms. Since most of the forcing points do not coincide with the immersed boundary interface, velocities and temperature had to be reconstructed and a quadric interpolation procedure (Tseng and Ferziger, 2003) involving points from fluid phase was carried out. This second-order interpolation is meant to preserve the scheme's accuracy. Similarly to velocity component treatment, an immersed boundary treatment is provided for the energy equation and the forcing energy term is added in the temperature Eq. (3):

$$\Phi^k = \frac{\theta_s - \tilde{\theta}^k}{\Delta t} - \mathrm{RHS}_\theta^k \tag{12}$$

where RHS_θ^k contains convective and diffusive temperature terms. In Eq. (12), $\tilde{\theta}^k$ (or θ_s) refers to the forcing location temperature helping to ensure the desired boundary condition. As for velocity components, most of the forcing temperature points do not coincide with the immersed boundary; an interpolation operator is consequently required and the technique of reconstruction used for velocity is also applied to preserve the same order of accuracy in the whole computational domain. The interpolation procedure is a single-step process that involves the three fluid points of each forcing point used by Yang and Balaras (2006). The interpolation procedure is a second-order linear interpolation and interpolation coefficients are estimated in the beginning of the simulation since we considered non-movable walls.

To model turbulence, large-eddy simulation has been carried out with a dynamic subgrid model to estimate the coefficients linking subgrid fluxes to resolved quantities. However, estimation of the C_s momentum coefficient and Pr_t subgrid Prandtl number at forcing points is by no means straightforward; evaluation of all the necessary test-filtered quantities, in the vicinity of the immersed boundary may include points within the solid and can lead to errors near the immersed boundary. To avoid complex modification of the filtering operators at these points and in order to estimate the quantities, a reconstruction procedure was applied for C_s and Pr_t. As regards, it is useful for wavy channels to access to wall quantities such as shear stress, wall friction and wall heat flux at the surface of the immersed boundary. In our estimation, a similar reconstruction method applied to velocity, pressure and temperature is introduced at surface control points. Concerning the pressure, the interpolation procedure renders it possible to force zero normal pressure gradients along the wavy walls.

2.3. Computational domain and mesh grid influence

The basic flow geometry is illustrated in Fig. 1b and all the configurations studied are summarized in Table 1. The computational domain is a $L_x \times L_y \times L_z$ box that fully integrates the wavy channel to study; the flow is assumed to enter into the wavy wall channel bounded by the two wavy surfaces considered as immersed boundaries. All mesh nodes outside these wavy surfaces are considered as embedded in the solid phase and consequently not taken into account. At inlet, constant velocity and temperature profiles are imposed in the streamwise direction while 2% white noise perturbation is applied on the velocity field. The outlet boundary conditions are considered thermally and dynamically as passive flow. The form of this condition was deduced by solving balance equations including convective and diffusive terms as well (Pham et al., 2006). Concerning lateral boundary conditions, a no-slip condition is imposed all along the two wavy walls by forcing all velocity components equal to zero through the reconstruction technique along the immersed boundary surfaces as just described. In addition, temperature along the wavy surface is assumed to remain at a constant level of 293 K throughout reconstruction technique. As concerns the transversal direction (z), periodic boundary conditions are applied. In the lengthwise direction, no periodic conditions were applied and eight wavy periods were simulated. This allows one to take into account not only the turbulent region but also the laminar steady and unsteady ones as well as transition towards turbulence (Blancher et al., 2004; Tafti et al., 2000). We extended up to 16 wavy periods for case 1 (not shown) in order to confirm flow field development especially in the turbulent region and all the trends obtained for eight wavy periods were confirmed with the 16 wavy period case.

Table 1
Configurations of simulations and grid parameters

Case	$\varepsilon = S/2A$	$\gamma = 2A/L$	$\alpha = S/H$	$L_x \times L_y \times L_z$	$N_x \times N_y \times N_z$
1	1.0	0.2	0	$8.0 \times 0.4 \times 0.3$	$2048 \times 320 \times 64$
1-M2	1.0	0.2	0	$8.0 \times 0.4 \times 0.3$	$1536 \times 240 \times 48$
2	0.803	0.267	0.637	$8.0 \times 0.43 \times 0.26$	$2048 \times 320 \times 64$
3	0.4	0.2	0	$8.0 \times 0.28 \times 0.3$	$2048 \times 320 \times 64$
4	0.6	0.2	0	$8.0 \times 0.32 \times 0.3$	$2048 \times 320 \times 64$
5	1.4	0.2	0	$8.0 \times 0.48 \times 0.3$	$2048 \times 320 \times 64$

All dimensions of the simulated cases and grid resolutions are listed on Table 1. The grid mesh dependency is naturally a key point and specific attention was paid to such point (Pham et al., 2003; Pham et al., 2008). To highlight that purpose, two grid mesh resolutions were studied (cases 1 and 1-M2). While the finer grid presents $y^+ = \frac{\rho u_\tau y}{\mu}$ of the order of magnitude 1.2 with more than five points within $y^+ < 10$, only two points are within that range. As a consequence, it was found that the f friction coefficient was better predicted with the finer mesh grid. For $Re = 3000$, the difference between numerical and experimental data was found to be equal to 4% and 8% for the finer and coarser grid, respectively. Such observation corroborates what Hanjalic (2004) recently put forward, i.e. LES technique is severely constrained by the near-wall resolution requirement especially when wall phenomena such as friction and heat transfer are placed into focus.

All the data shown hereinafter were obtained with the finest grid mesh resolution, i.e. simulations were conducted on a $2048 \times 320 \times 64$ mesh grid. The non-dimensional time between each time step was programmed to set the Courant number at less than 0.3. Our numerical model was implemented on an IBM cluster machine and computations were performed on 16 parallel processors. Characteristic CPU time on that machine for one run is equal to approximately 3200 h per configuration.

3. Results and discussion

3.1. Global flow characterization

We began by studying a wavy channel geometry characterized by a ε spacing ratio and γ waviness aspect ratio of 1.0 and 0.2, respectively. To depict flow field behaviour that takes place in a wavy channel, it is interesting to identify the existence and behaviour of structures that develop all along the channel. One should initially recall the fact that several experimental analyses have already been conducted to investigate the flow regime in wavy channels. Among these works, Rush et al. (1999) analysed 12–14 periods in detail and took into account the influence of wavy

channel amplitude, spacing ratio and phase angle between the two wavy walls. With an experimental technique, Rush et al. managed to identify the passage from laminar to unsteady laminar by paying close attention to the onset of macroscopic mixing. Since their experiments were limited to a Reynolds number lower that $Re = 1000$, transition from unsteady laminar to turbulence did not occur. In addition, one should remind that from an experimental point of view 3D behaviour identification is not an easy task. As we endeavoured to numerically detect instability growth and transition mechanism from laminar to turbulence, we initially selected a way of identifying these structures. A number of techniques for the identification of vortices have been put forward, and they are mainly derived from either on local clustering of vortex lines (Kim et al., 1987), or from elongated regions of low-pressure regions with velocity tensor complex eigenvalues (Chong et al., 1990) or else from the second invariant of the velocity gradient tensor (Hunt et al., 1988). All of the methods listed above are powerful in capturing signatures of the vortex and have proven

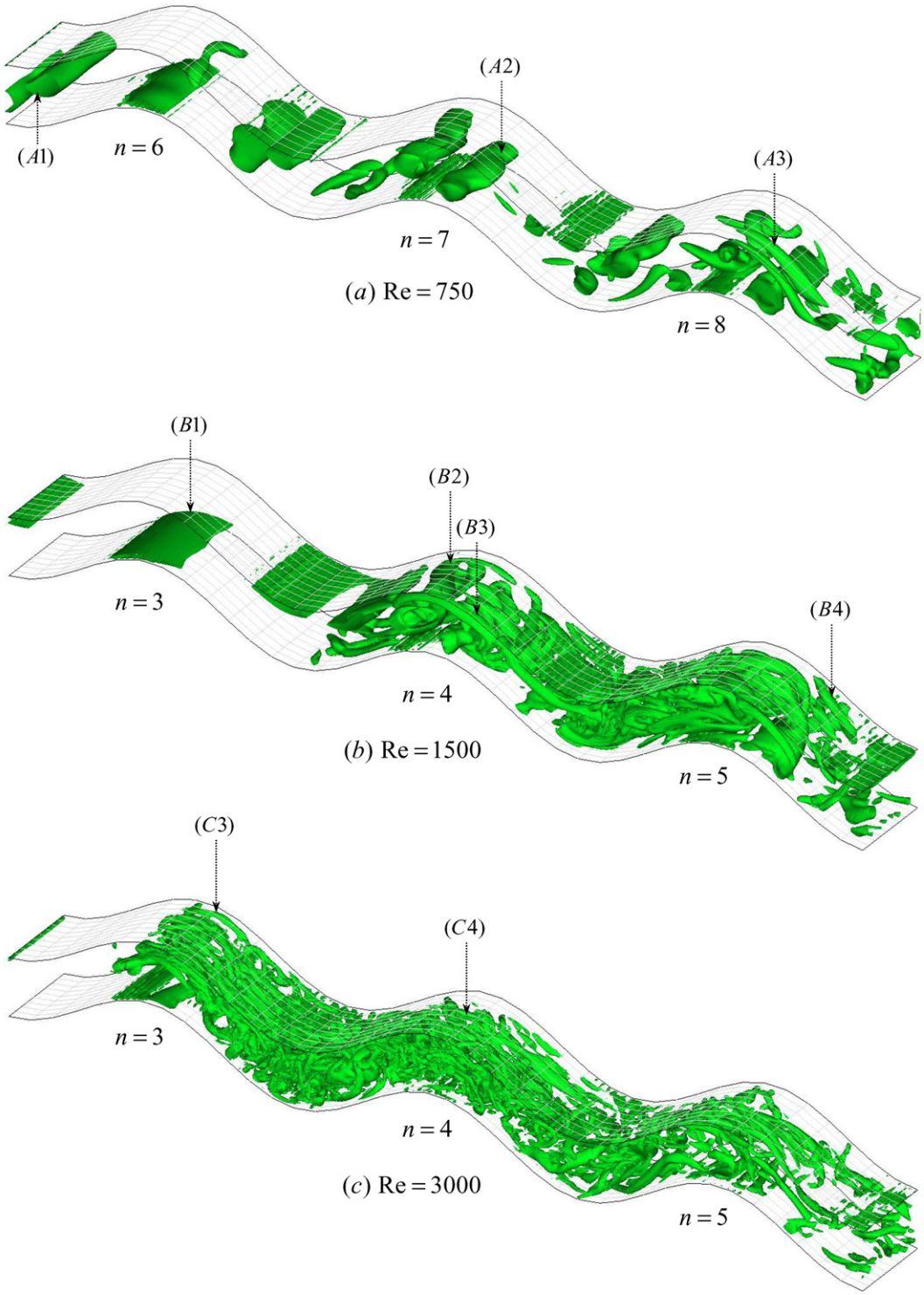

Fig. 2. 3D iso-surface distribution of λ_{ci}^2 with regard to different Reynolds numbers.

successful in flow situations. On this subject, we follow Chong et al. (1990) in their general classification of the three-dimensional velocity field around a critical point. Then, when visualizing vortices, we refer to the imaginary part of the complex eigenvalue of the velocity gradient tensor. This method of vortex tracking was applied to our numerical data for different Reynolds number levels (Fig. 2). In fact, Fig. 2 shows pseudo three-dimensional isocontours corresponding to 5% of the maximum value of the square imaginary part of the complex eigenvalue (λ_{ci}^2). At first glance, the vortex structures developed in the wavy channel flow are significantly dependent on the Reynolds number and wavy period considered. For $Re = 750$, several vortex topologies have been identified; two-dimensional vortex tubes (A1) first developed along wavy period 6 and it clearly demonstrates that the flow field becomes unsteady from that location; note that upstream from wavy period 6, no structures are generated and the flow remains steady. These 2D connected tubes develop in the wake of crest (trough) for the lower (upper) wavy wall and during their convection, structures are more or less stretched out, resulting in the structure topology A2: structures in the wake of the crest (trough) are still connected in the spanwise direction but the tube is significantly distorted from wavy period 7. As expected structures identified along the next wavy period are profoundly altered and mainly three-dimensionally organized. As clearly identified along wavy period 8 (Fig. 2), structure development becomes strongly elongated in the lengthwise direction (A3) favouring three-dimensional structures. This process seems to indicate the start of the transition process from laminar unsteady to more turbulent behaviour. Note that spectral analyses (not shown) do not reveal any well-known $-5/3$ power-law distribution underlining the fact that turbulence is not yet achieved at that Reynolds number. For $Re = 1500$, this process seems to occur sooner spatially. In fact, along wavy period 3, shear along the crest (trough) along the lower (upper) wavy wall is so strong that no 2D connected tubes are identified and on the contrary, only very thin regions of λ_{ci}^2 are periodically identified (B1). The rapid growth of instability is highly apparent, and along wavy period 4, distorted 2D vortex tubes are detected (B2) but the latter transit towards elongated tubes in a lengthwise direction similar to that observed in the transition process depicted for $Re = 750$. In addition, wavy periods 4 and 5 reveal

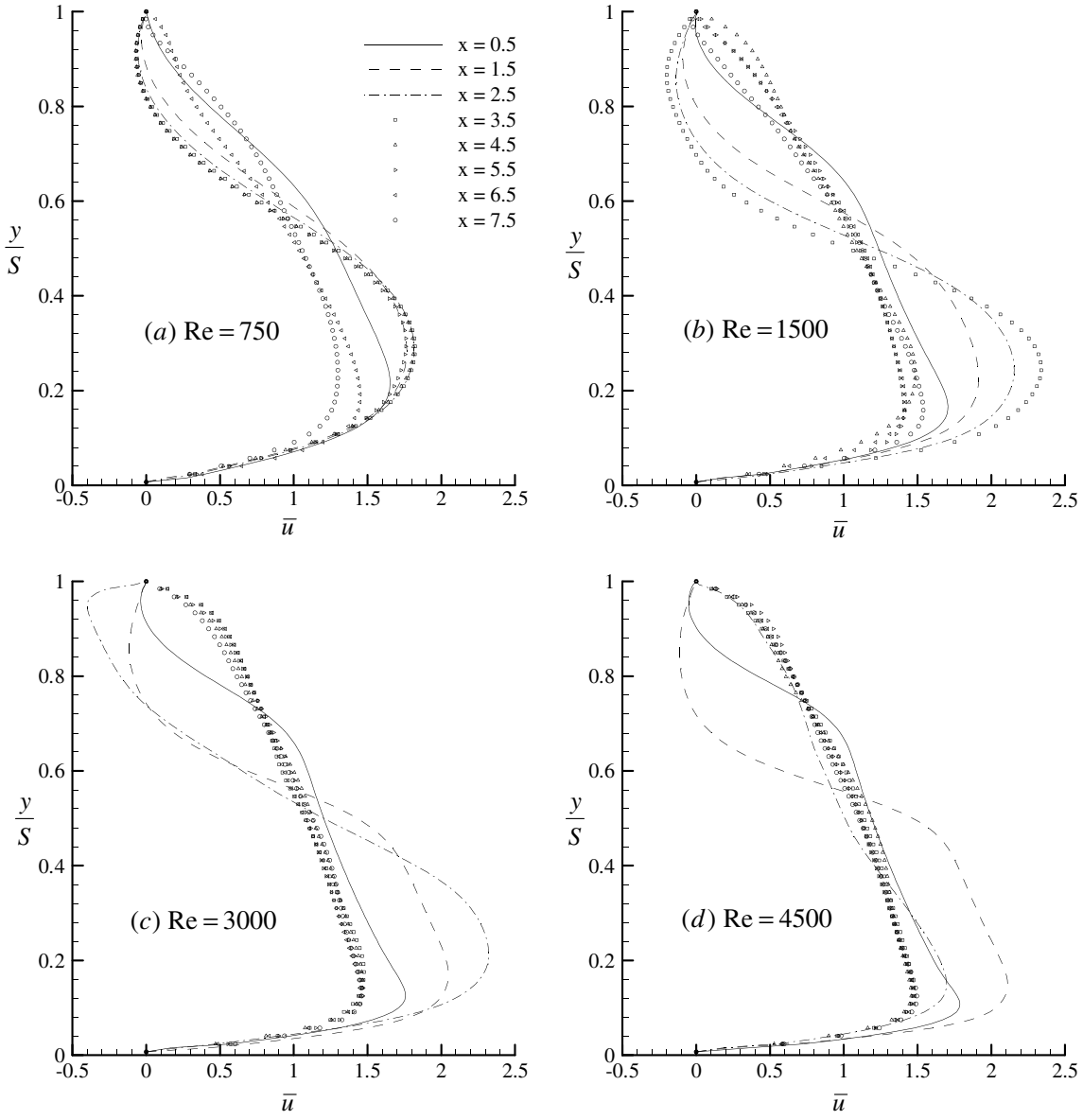

Fig. 3. Non-dimensional streamwise velocity profiles at crests along the lengthwise of the wavy channel for *Re* Reynolds numbers of 750, 1500, 3000 and 4500.

a large concentration of vortices mainly organized as elongated vortex tubes in the lengthwise more or less interlaced in the rear part of wavy period 5; these elongated vortex tubes seem literally to have been stretched into smaller and disconnected structures (B4). The process depicted for $Re = 1500$ is similar to what is observed for $Re = 3000$ except that these vortex structure developments arise sooner spatially.

In order to better depict how flow field behaves with regard to *Re* Reynolds number, profiles at crest (for the lower wavy wall) of the mean streamwise velocity for several *Re* levels are shown in Fig. 3. As clearly stated in the boundary condition section, each simulation is conducted with a flat inlet velocity profile, and it is obvious that the first wavy period passage strongly alters the velocity flow field. As we compared velocity at crest, maximum velocity amplitude is detected in the lower part of the wavy channel while low velocity amplitude and even negative levels are detected in the upper part of the channel. At first glance, velocity profiles converge towards a similar shape along the lengthwise whatever the *Re* level but the length required to achieve it is naturally linked to *Re*; the higher *Re*, the less the length. In fact, one may consider self-similarity as pretty much achieved at $x \sim 6.5$, 5.5 and 3.5 for $Re = 750$, 1500 and 3000, respectively. Note that for higher Reynolds numbers, i.e. for $Re = 4500$, self-similarity is reached at $x = 3.5$ as well. Naturally, such an observation was to be expected, since we had identified vortices and coherent structures along the wavy channel (Fig. 2). Furthermore, it is necessary to underline that self-similarity velocity profiles reveal shapes that are linked to *Re*. For $Re = 750$, velocity profiles are not fully similar at $x = 6.5$ and 7.5 but both of these profiles are mainly characterized by an increase up to $y/S \sim 0.2$. For $0.2 \leqslant y/S \leqslant 0.7$, the velocity goes down almost linearly and in the upper part of the channel, the decrease is much more strongly accentuated due to the non-slip condition at $y/S = 1.0$. However, for higher *Re* levels, velocity gradients close to the walls are naturally higher and profiles evolve for $Re = 1500$ and even 3000. The flow regime appears to be fully established and self-similarity occurs. For this Reynolds range, velocity profile shape is mainly characterized by significant gradients above the lower wavy wall and maximum velocity amplitude is reached very close to the wavy wall; then velocity evolves almost linearly to abruptly drop to zero in the vicinity of the upper wall. As did Henn and Sykes (1999), we normalized velocity amplitude with u_τ friction velocity and plotted the data with regard to y^+ (not shown) and it was found that the first velocity node calculated was at worse at $y^+ = 1.2$, i.e. that confirms at *posteriori* the ability of the mesh grid to deal with turbulent boundary layer.

To study flow field fluctuating activity, we have followed the modification in the turbulent dynamic and thermal intensity that are defined as $I_u = \sqrt{\overline{u'^2} + \overline{v'^2} + \overline{w'^2}}$ and $I_t = \sqrt{\overline{\theta'^2}}/\bar{\theta}$, respectively. Fig. 4 shows the change of $\bar{I}_u$ and $\bar{I}_T$ cross-section average turbulent intensities with regard to the *x* lengthwise location. The changes of $\bar{I}_u$ and $\bar{I}_T$ along the wavy periods are shown in Fig. 4 for the four Reynolds numbers and it is strikingly interesting to note similarities in the behaviour for the two highest Reynolds number shown (i.e. for $Re = 3000$ and 4500). Actually, $\bar{I}_u$ levels are initially close to zero in the first two periods while an abrupt increase at the end of period 2 and at the beginning of period 3 occurs and a maximum peak is reached at $x = 2.4$ and 2.8 for $Re = 4500$ and 3000, respectively. The maximum reached is higher than 60% for both *Re* values. As soon as this happens, the amplitude of $\bar{I}_u$ decreases asymptotically and converge towards a constant level close to approximately 30%; even if $\bar{I}_u$ evolves here and there from that constant along the wavy channel, one may conclude that no significant change occurs at these two Reynolds numbers. Taking into account the structure

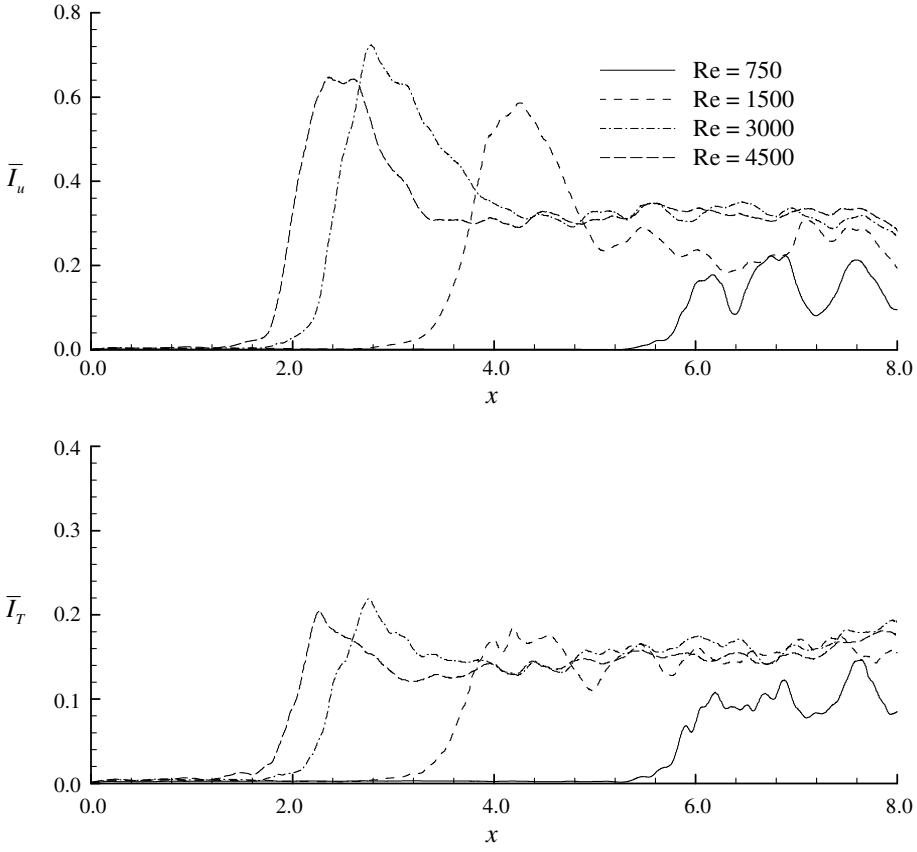

Fig. 4. $\bar{I}_u$ and $\bar{I}_T$ cross-section and time-averaged dynamic and thermal turbulent intensities change with regard to *x* for different Reynolds numbers.

identification part, the $\bar{I}_u$ peak is identified in a region where unsteady development occurs, more specifically where 2D tubes as well as 3D structures arise. In addition, the development of the smallest 3D complex structures directly corresponds to the region where $\bar{I}_u$ reaches its constant level of 30%. Everything occurs as if it corresponds to the transition mechanisms and once $\bar{I}_u$ remains at a constant level, this indicates that flow field is turbulent. Actually, in order to determine whether or not the flow is turbulent, we have analyzed the density spectral power (not shown) of the velocity fluctuations for $Re = 3000$ and 4500, and the well-known $-5/3$ power-law is clearly present for $x \geqslant 5.0$. As shown in $\bar{I}_T$ distribution (Fig. 4), its evolution with regard to x lengthwise location is similar to that observed for $\bar{I}_u$, i.e. increase from $x \sim 2.0$ to reach a maximum $\bar{I}_T$ turbulent thermal intensity while up to that maximum, $\bar{I}_T$ asymptotically tends to a constant level close to 16%. For $Re = 1500$, this typical shape is likewise observed and an increase of $\bar{I}_u$ and $\bar{I}_T$ occur close to $x \sim 4.0$. Thus, while an almost constant level is reached for $x \geqslant 6.0$ for $\bar{I}_T$, significant changes are still detected for $\bar{I}_u$. As no clear $-5/3$ power-law in the fluctuating field may be detected, we speculate that at $Re = 1500$, the flow field is mainly unsteady but turbulence is not established. However, under these conditions, a transition may occur and in order to check it, one should first enlarge the computational domain. Concerning $\bar{I}_T$ and $\bar{I}_u$ for the lowest Reynolds number shown, significant decrease in the fluctuating fields occurs; no clear maximum is observed and the turbulent fluctuating intensities vary widely. So as to determine whether or not under this condition the flow remains laminar, specific calculations should be undertaken even though as put forward by Rush et al. (1999), structures that develop for low Reynolds numbers cannot be assimilated to a transition process from laminar to turbulence but rather as "mixing onset jump" from one wavelength to another one which does not necessarily imply turbulence. In addition, from Rush et al.'s experimental data, critical Reynolds number from laminar to laminar unsteady was found to vary from 200 to 800 but the critical number is naturally strongly linked to the geometrical configuration. We speculate that $Re = 750$ is below the critical Reynolds number, i.e. flow does not transit to turbulence. Precise determination of critical Reynolds for the case studied is obviously a worthwhile objective but does not correspond to our main goals. We have rather decided to continue to detail heat and mass transfer for the given Re Reynolds numbers.

One should nonetheless not forget that all the mechanisms identified above have a dramatic impact on the heat transfer efficiencies. In addition, even if large-eddy simulation was found to be an accurate method to depict flow field over a wavy surface, validation is always required. So, as did Zhang et al. (2003), the numerical validation was conducted by directly comparing experimental and numerical f Fanning factor and j Colburn factor changes with Re. To do so, we first estimate these two factors along each period that constitutes the whole wavy channel. f Fanning factor is obtained from:

$$f = -\frac{\mathrm{d}p}{\mathrm{d}x}\frac{D_h}{2\rho U^2} \tag{13}$$

while a thermal balance is applied on each wavy period to estimate Nu Nusselt number defined as

$$Nu = \frac{\dot{m}c_p(T_{m,o} - T_{m,i})D_h}{kA_h\Delta T_m} \tag{14}$$

where the mean temperature may be defined as

$$T_m = \frac{\int T(y,z)u\,\mathrm{d}y\,\mathrm{d}z}{\int u\,\mathrm{d}y\,\mathrm{d}z} \tag{15}$$

and the log-mean temperature difference ΔT_m may be defined as

$$\Delta T_m = \frac{(T_w - T_{m,o}) - (T_w - T_{m,i})}{\ln[(T_w - T_{m,o})/(T_w - T_{m,i})]} \tag{16}$$

Thermal heat transfer was characterized by the j Colburn factor ($j = Nu/RePr^{1/3}$).

Fig. 5 shows the change of f Fanning factor and j Colburn factor computed for each wavy period along the streamwise direction. Actually, in line with what we stated above, it is obvious that the j and f changes are intimately linked to several flow field behaviors occurring along the wavy channel. In the first wavy periods where flow field is laminar, f presents high levels for a low heat transfer exchange. Actually, in the first two wavy periods, the first four and even six for $Re \geqslant 3000$, $Re = 1500$ and 750, respectively, flow field behaves as steady and the two j and f parameters do not markedly evolve. This is no longer true anymore as soon as unsteadiness develops. For the highest Reynolds studied (i.e. for $Re = 3000$ and 4500), j is increased by a factor of 2 evolving from 0.006 in the first two periods to 0.012 in the transition region ($n = 3$). At the same time, f is reduced resulting in local improvement of the j/f efficiency. Note that significant variations in j and f levels from one period to the other in that region are exhibited and that even if they are not particularly pronounced, they still exist in the turbulent region or the unsteady region. For the highest Re Reynolds number shown of which turbulent region is clearly identified, j and f remain at almost constant levels even if some slight variations from one wavy period to the other may occasionally be noticed. We improved the temporal integration by a factor of 1.5 but these variations still remained. From our point of view, they due simply to the fact that the whole flow field continuously evolves along the wavy channels. In the turbulent region, the heat transfer coefficient is about two times higher than levels reached in the steady region; concerning the f Fanning coefficient, a decrease of the latter by a factor of 2 is also detected; consequently, overall j/f efficiency is about four times higher in the turbulent than in the steady region. It is also interesting to underline that j is strongly enhanced for low Re numbers and that maximum levels reach up to 0.03, i.e. that is to say up to 2.5 times higher than levels reached for $Re \geqslant 3000$. At the same time, f reaches similar levels for lower Reynolds numbers than for $Re \geqslant 3000$, thereby highlighting the potentiality of heat and mass transfer in that Reynolds range.

In order to validate our numerical simulations, we decided to take into account the geometrical configuration experimentally and numerically studied by Zhang et al. (2003). It is characterized by α, γ and ε parameters equal to 0.637, 0.267 and 0.803, respectively. Our numerical simulations were carried out on a similar grid mesh resolution similar to that used for the three Reynolds numbers ($Re = 1500$, 3000 and 4500); further numerical details are listed in Table 1. Note that contrarily to most of the simulations shown in the literature, our validation simulations took into account a finite channel height in order to fully simulate the geometry proposed by Zhang et al. (2003). Our numerical results for the average heat and friction coefficients are shown in Fig. 6, in which the variations in j and f with Re are plotted. We also included numerical and experimental data extracted from Zhang et al. (2003); as stated by the authors, an extrapolation of numerical predictions was useful in comparison with experimental data because the Reynolds ranges were different; Zhang et al. numerical simulations were limited to $Re \leqslant 1500$ while their experience was conducted in the range of $1000 \leqslant Re \leqslant 7000$. So, as can be clearly observed in Fig. 6, we computed the Zhang et al. configuration for three Reynolds numbers that fall within the experimental range. From the data shown, it is obvious that the heat transfer coefficient is perfectly estimated and fit the experimental data. Whatever the Re level, the difference between prediction and experimental data was at worse lower than 4%. On the other hand, agreement in the f factor is not as satisfactory; the differences

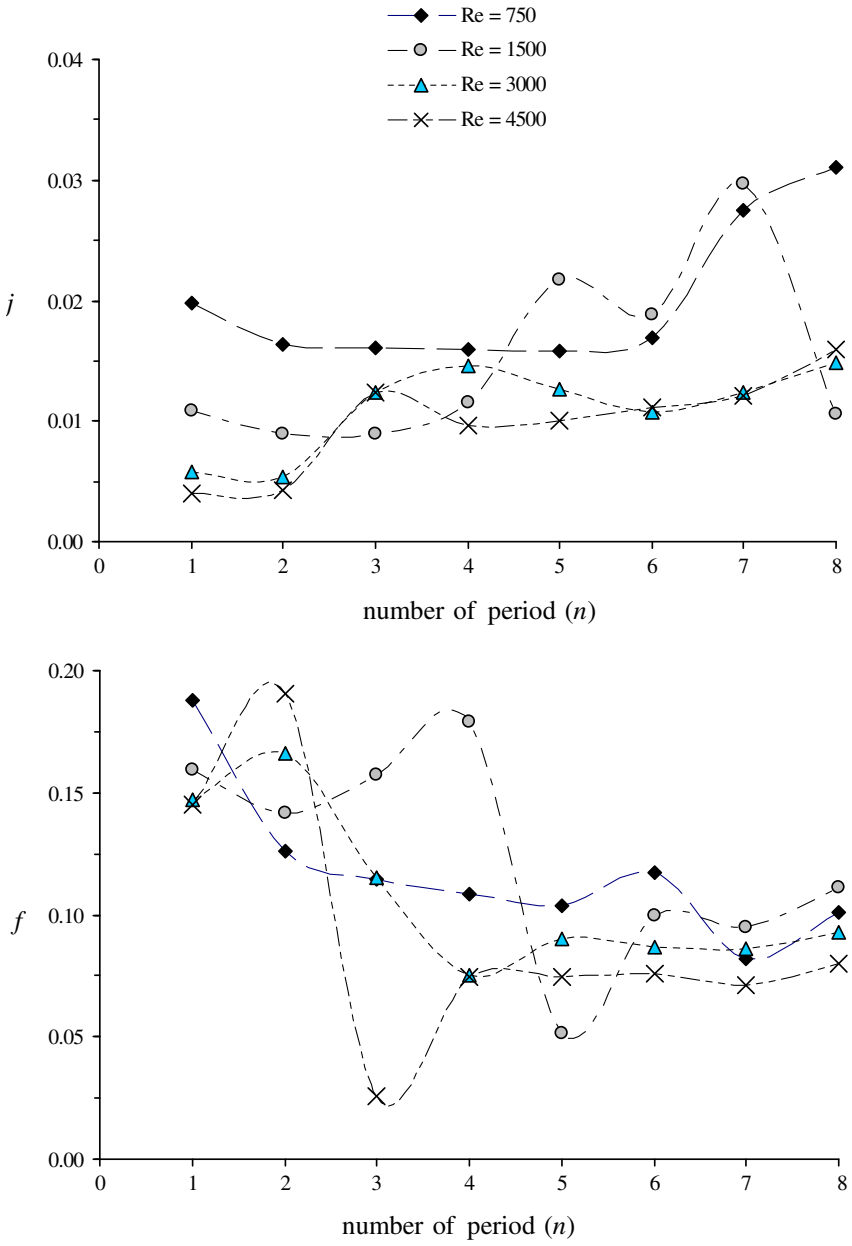

Fig. 5. j heat transfer coefficient, f friction factor, f change along each wavy period and for different Reynolds numbers.

between prediction and experiments increase with *Re* and are found to be equal to 2%, 8% and 14% for *Re* = 1500, 3000 and 4500. From our point of view, numerical predictions were accurate enough to allow us to affirm that our numerical simulations are validated.

3.2. Influence of ε channel spacing ratio

The influence of sinusoidal wavy surface plate-fin geometry and especially the channel spacing ratio was numerically investigated. As underlined in the introduction, several numerical analyses were conducted on the turbulent flow structure development on wavy surfaces, and one of our objectives is to shed light on the wavy top wall influence on the whole flow field behaviour. Fig. 7 shows the y/S lateral profiles of the normalized longitudinal velocity component for three different ε spacing ratio along wavelengths 5, 6 and 7; these wavelengths were selected because turbulent flow field was fully established whatever ε studied at *Re* Reynolds number of 3000. Table 1 lists the complete characteristics of the different numerical cases studied. Location of transition from laminar to turbulence was performed similarly to the previous part, i.e. by simultaneously analyzing the longitudinal change of turbulent intensities as well as three-dimensional turbulent structure behaviour. Transition was found to occur (not shown) from wavelength 3 for $\varepsilon = 1.4$, 1.0 and 0.6. Eight profile locations are shown from crest to crest. As can be clearly observed at first wave crest ($x/\lambda = 0$), velocity profiles reveal a maximum just above the crest for $\varepsilon = 1.0$ and 1.4; once this maximum is reached, the velocity first decreases slowly with the increase of y/S up to $y/S = 0.5$ while above that position, the longitudinal velocity decrease is much more pronounced. This trend is similarly observed for $\varepsilon = 1.0$ the maximum peak is more highly located in the channel and smaller in amplitude. However, the changes with regard to ε are much more significant for $\varepsilon = 0.6$ for which the velocity profile at $x/\lambda = 0$ is almost flat in most of the channel height, i.e. $0.15 \leqslant y/S \leqslant 0.9$; in fact, there is a slight decrease in this region which is quite linear from the bottom

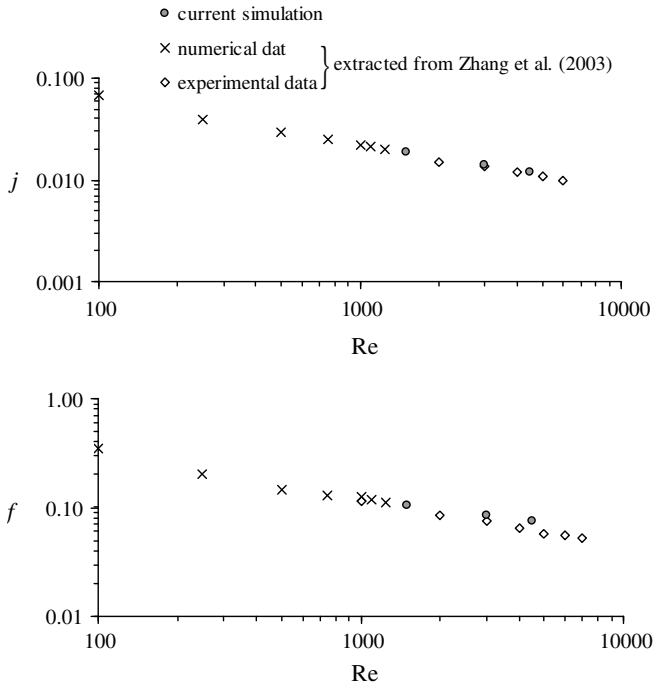

Fig. 6. Global variations of j heat transfer coefficient, f friction factor versus Re Reynolds numbers for a wavy channel configuration of ($\varepsilon = 0.803$, $\alpha = 0.637$ and $\gamma = 0.267$) and comparison to available data.

to the upper wall. Between the crest and the trough, average velocity profiles drastically evolve especially for $\varepsilon = 1.0$ and 1.4. The maximum longitudinal velocity is always detected at least for $\varepsilon = 1.4$ but the latter has shifted from the lower to the upper part of the channel. This shift is then completed at the trough where the velocity profile is symmetrically similar to the one observed at the downstream crest. While these changes are remarkably pronounced for $\varepsilon = 1.0$ and 1.4, those along the wavelength for $\varepsilon = 0.6$ are smoother but still exist with a similar shift of the maximum velocity level from the bottom to the top of the channel. From average velocity profiles, it appears clearly evident that the smaller ε, the more flow field is longitudinally oriented, i.e. velocity profiles are smoother. Considering velocity gradients, significant shear is induced very close to the walls and there exist regions, as depicted above, where shear develops in the main flow field as well. In addition, there are some regions with negative longitudinal velocities, i.e. reverse flow occurs. Actually this reverse flow field behaviour is mainly observed at down-slope (i.e. up-slope) locations for lower (i.e. upper) walls for $\varepsilon = 1.4$ and to some extent for $\varepsilon = 1.0$. To highlight the development of reverse flow, one simply needs to follow velocity profiles between $x/\lambda = 0.2$ and 0.4 for $\varepsilon = 1.4$; along this spatial area close to the lower wall, longitudinal velocities are negatives. Numerical results indicate that the reattachment point is somewhat further downstream from $x/\lambda = 0.7$, i.e. along the up-slope wall.

To analyse the influence of ε on flow field behaviour, we may study higher-order statistics by following first the I_u turbulent velocity intensity. I_u turbulent intensity profiles have been plotted in Fig. 8 at similar locations similar to those used for longitudinal velocity profiles in the last figure. At first glance and for $Re = 3000$, turbulent activity is directly influenced by the ε spacing ratio and the higher ε the higher are I_u levels. To go into detail, I_u profile at crest (i.e. $x/\lambda = 0.0$) for $\varepsilon = 1.4$ reaches turbulent levels higher than 50% for $y/S \sim 0.7$, i.e. in the upper channel part where average velocity is significantly sheared as just shown before. In the lower part of the channel, I_u remains an almost constant level describing a plateau of constant level equal to 30%. To correlate I_u and longitudinal velocity profiles at crest, it is obvious that I_u is more pronounced in the upper part of the channel where significant decrease of velocity induces shear that creates turbulence. Thus, as expected for lower spacing ratio, I_u profiles for $\varepsilon = 1.0$ are similar to the one observed for $\varepsilon = 1.4$ but turbulent maximum peak is lower and close to 40% while in the lower part, I_u is lower than the constant level reached for $\varepsilon = 1.4$. While considering I_u distribution at the crest for $\varepsilon = 0.6$, its distribution is smoother than for the two previous spacing ratio shown and maximum levels are also significantly reduced, reaching only 25%. To conclude, average velocity profiles were found to be more homogeneous with smaller lateral changes providing them with weaker turbulent activity. Along the wavelength, the I_u turbulent intensity profiles drastically evolve for $\varepsilon = 1.0$ and 1.4 while for $\varepsilon = 0.6$, the changes are not so pronounced. For $\varepsilon = 1.4$, the maximum peak detected at the crest is still present at $x/\lambda = 0.2$ in the upper part of the channel but a secondary and lower peak develops at $y/S \sim 0.15$ approximately. This secondary peak rapidly evolves and becomes predominant at $x/\lambda = 0.4$ reaching levels close to 50%; at that location, the lower part of the channel corresponds to an area where maximum turbulent activity occurs while in the upper part, fluctuating activity is strongly reduced but remains at a high level ($\sim$30%). This trend develops up to $x/\lambda = 0.7$, i.e. along the down-slope and up to the mid-up-slope as well. This behaviour is likewise clearly detected for $\varepsilon = 1.0$ and to some extent for $\varepsilon = 0.6$; however, for the smallest spacing ratio studied, it is clear that turbulent intensity is more homogeneous along the channel. Flow is clearly forced to flap between the upper and the lower wavy-slope, inducing shear-layer in which complex mechanisms arise. In addition, the smaller ε the more such flapping phenomenon is reduced. According to Henn and Sykes (1999), flow over a wavy surface is mainly characterized by a dramatic increase in the lateral velocity variance in a highly localised area close to the surface on the up-slope of the wave. On a wavy channel, as can be observed in the I_u turbulent intensity shown (Fig. 8), it is obvious that a strong increase in turbulent activity in the lower part of the channel occurs downstream from the trough. However, it is necessary to more closely analyse the change in the three different fluctuating velocity components all along the wavy-length period. Fig. 9 shows the contours of the three $\sqrt{\overline{u'^2}}$, $\sqrt{\overline{v'^2}}$ and $\sqrt{\overline{w'^2}}$ fluctuating velocity components along wavy period 5 in mid-plane for $\varepsilon = 0.6$ and 1.4; there are some strikingly noticeable differences in turbulence distribution with regard to the spacing ratio. $\sqrt{\overline{u'^2}}$ increases significantly on both sides of the trough location along the lower wall, i.e. $0.4 \leqslant x/\lambda \leqslant 0.8$ for $\varepsilon = 1.4$ while an increase of $\sqrt{\overline{u'^2}}$ occurs downstream from the trough for $\varepsilon = 0.6$. The transversal fluctuating activity mainly develops in the trough along the lower wall and in the crest along the top wall for $\varepsilon = 1.4$ while lateral fluctuating activity is still significant all along the wave length even if $\sqrt{\overline{v'^2}}$ increases at crest and trough. Concerning transversal fluctuating activity, $\sqrt{\overline{w'^2}}$ is significantly amplified along the up-slope (i.e. the down-slope) for the lower (upper) wall for $\varepsilon = 1.4$; this is the opposite for $\varepsilon = 0.6$ where $\sqrt{\overline{w'^2}}$ is amplified downstream from trough along the lower wall and upstream from trough for the upper wall. In addition, what surely constitutes one of the most significant differences between a wavy channel and a flow over a wavy surface is surely constituted by the $\sqrt{\overline{w'^2}}$ spatial evolution. As just noted, a wavy surface was found to significantly favour transversal fluctuating activity, which was the dominant component, exceeding even streamwise component fluctuating activity. In a wavy channel, $\sqrt{\overline{w'^2}}$ is always close or even lower than $\sqrt{\overline{u'^2}}$ levels reached whatever ε. Second, location of $\sqrt{\overline{w'^2}}$ production also strongly depends on the ε spacing ratio.

To qualitatively point out the effect of the channel height on the flow field, vortex structures were identified by following the

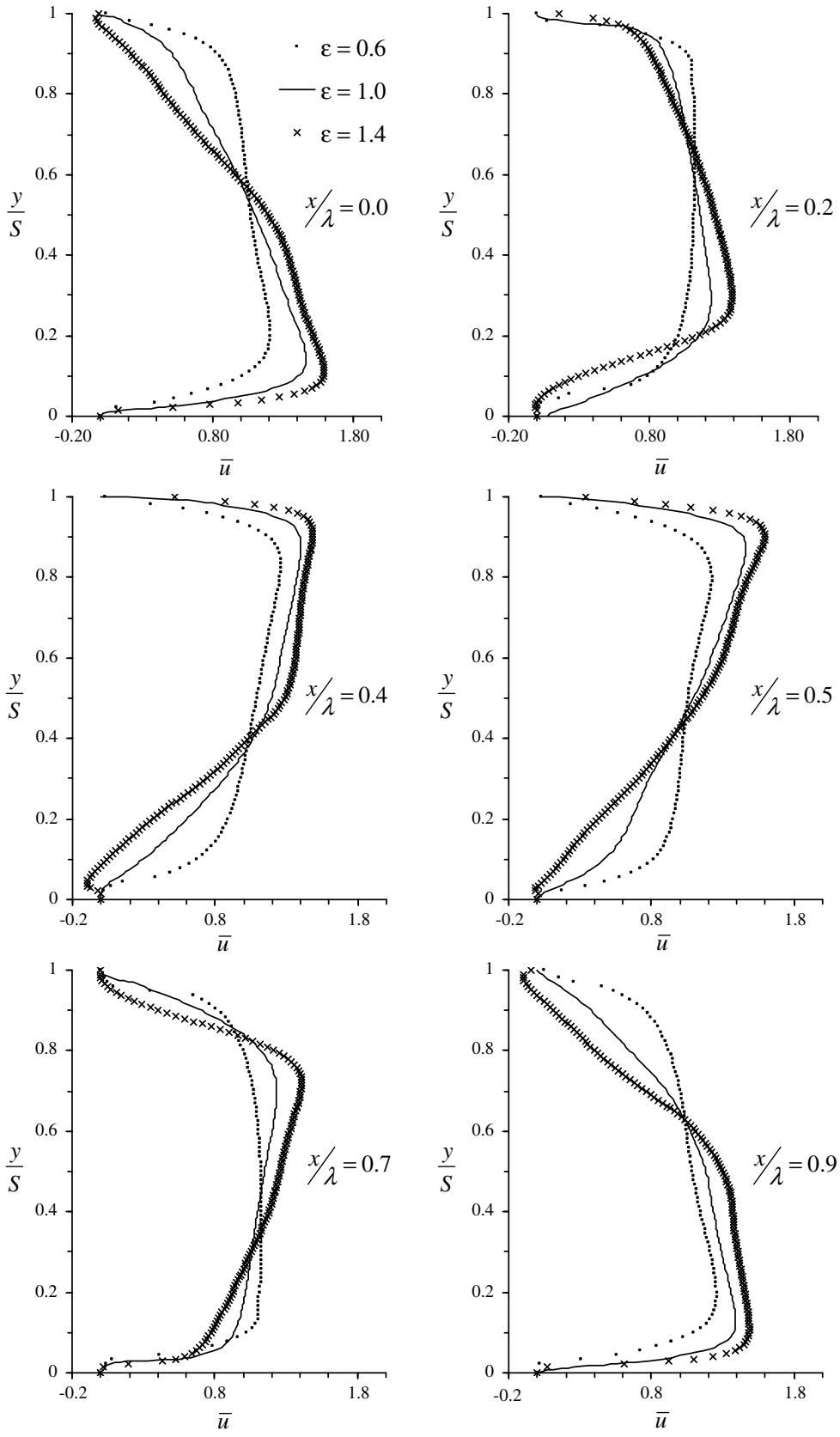

Fig. 7. Non-dimensional streamwise velocity profiles along wavy period 5 (from crest to crest) with regard to ε spacing ratio for $Re = 3000$.

iso-contour of λ_{ci}^2. Fig. 10 shows vortex identification along wavelengths 4 and 5 for $\varepsilon = 0.6$, 1.0 and 1.4. It is obvious that as expected, the trough along the lower wall and the crest along the upper wall are regions of significant vortex production. As vortices are created on both sides of the wavy walls, interactions between structures arise. To highlight the point, it is necessary to observe

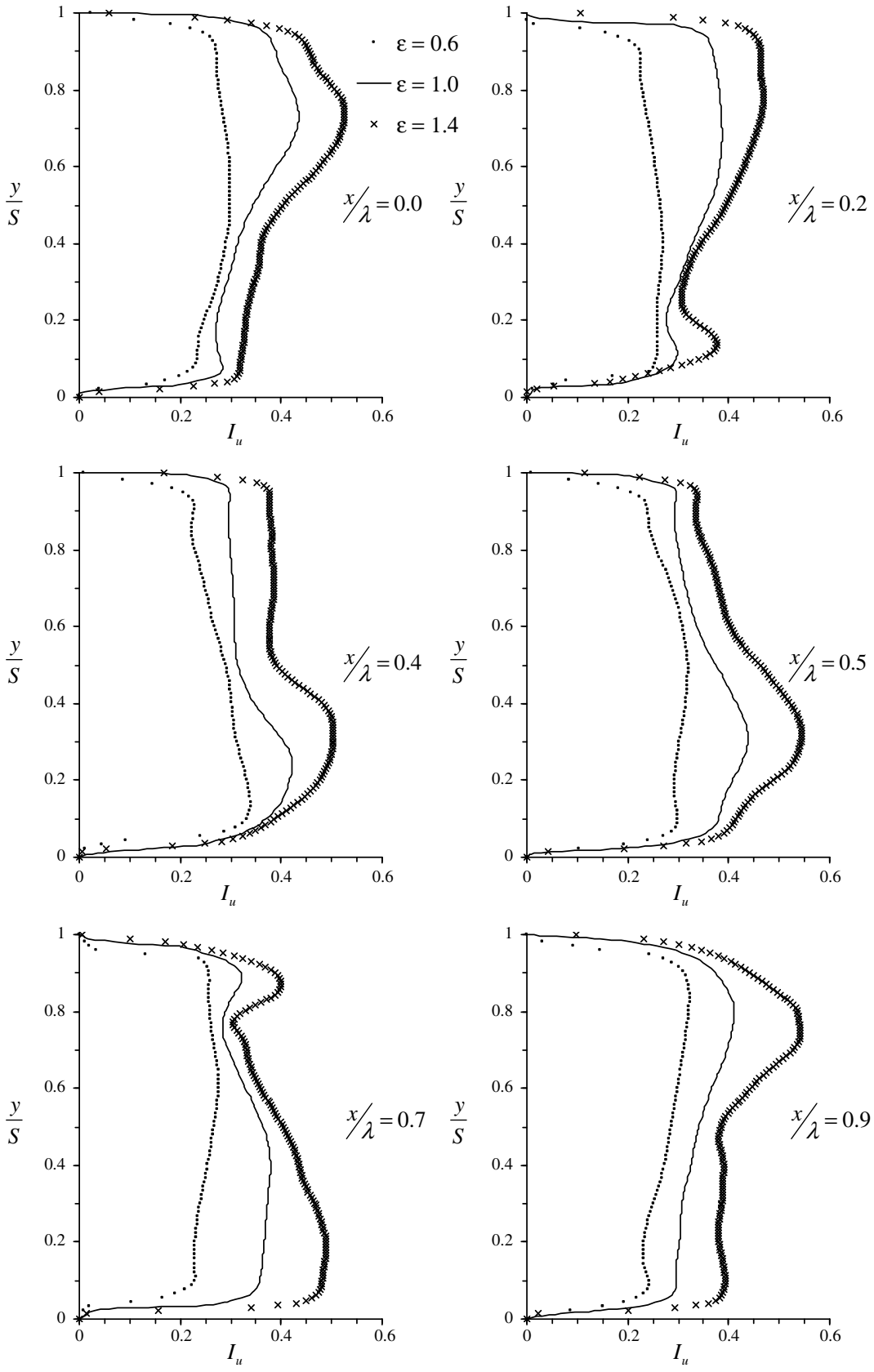

Fig. 8. Dynamic turbulent intensity profiles (I_u) along wavy period 5 (from crest to crest) with regard to ε spacing ratio for $Re = 3000$.

structures for $\varepsilon = 1.4$ from which the two wavy walls are sufficiently far as to clearly distinguish formation of structures along upper and lower walls. Structures arising from both top and bottom walls meet somewhat further upstream from the trough, thereby illustrating the structure interconnection process. This trend is observed as well for $\varepsilon = 1.0$ as well, but narrower wavy

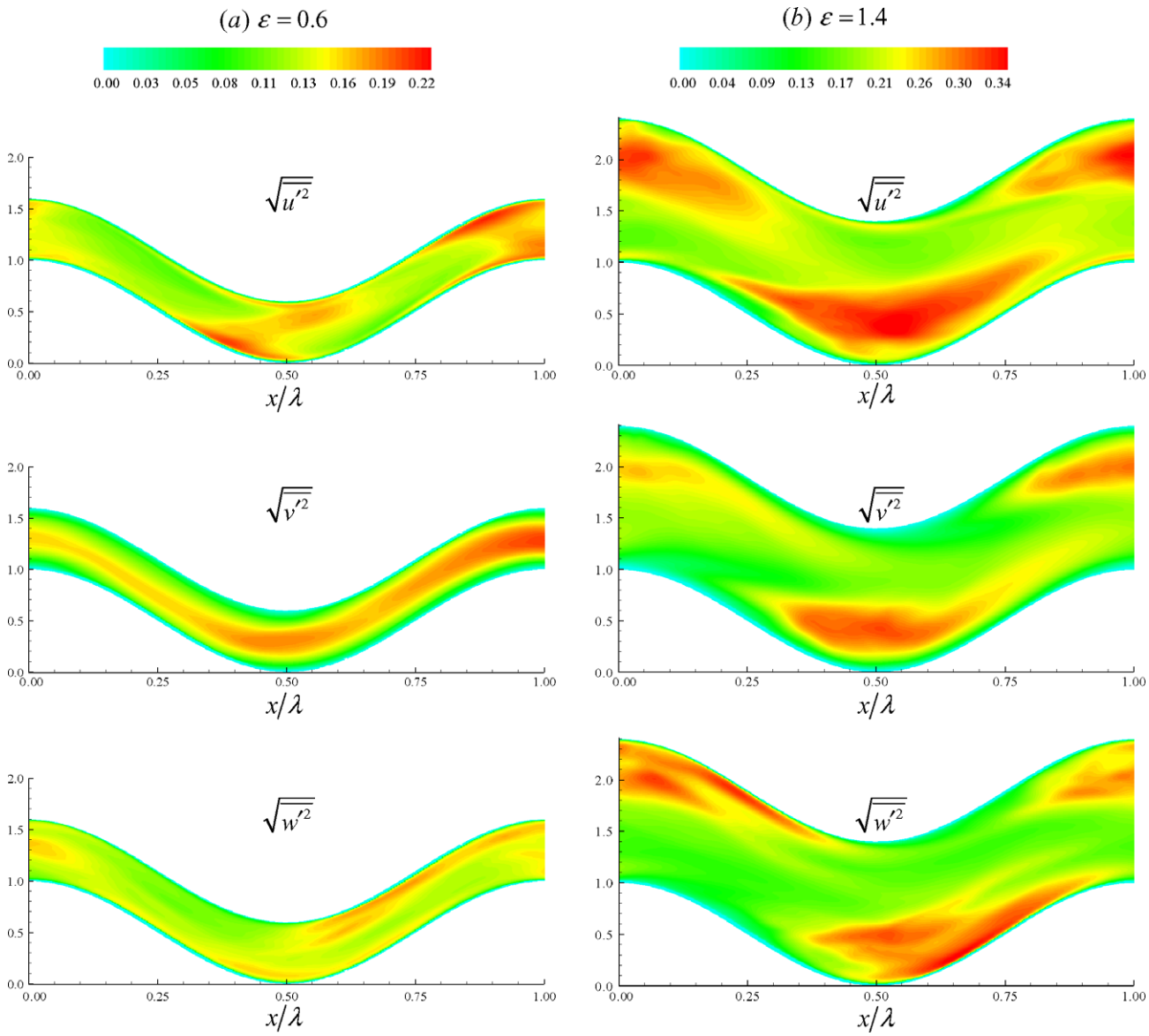

Fig. 9. Contours of the fluctuating velocity $\left(\sqrt{\overline{u'^2}}, \sqrt{\overline{v'^2}}, \sqrt{\overline{w'^2}}\right)$ along wavy period 5 for two spacing ratios ($\varepsilon = 0.6$ and 1.4).

walls are directly involved in vortex distribution; the structures appear to be more elongated and stretched for $\varepsilon = 1.0$ than those observed for a higher spacing ratio. This trend is remarkably accentuated for $\varepsilon = 0.6$. Along the lower wall, significantly elongated structures still keep their own identity along the down-slope. For small ε ratio, i.e. for $\varepsilon = 0.6$, structure production appears all along the wavy-length. Everything occurs as if the confinement imposed by the two wavy walls were reducing breakdown of structures created along up-slopes; while increasing velocity gradients all along the wavy walls, it also favours structure development.

From a more quantitative point of view, turbulent kinetic energy (TKE) budget was carried out. Resolved TKE q^2 is defined as

$$q^2 = \frac{1}{2} u_i'' u_i'' \tag{17}$$

where the double-prime quantities represent the difference between the resolved fluctuating quantity and the time mean of that quantity. To derive an equation governing $\langle q^2 \rangle$, one simply needs to subtract the mean momentum equation from its averaged form, multiply by u_i'' and average in time. Then, the TKE budget can be written as

$$\langle \dot{q}^2 \rangle = T_m + P + T_t + T_{sgs} + \beta + D_p + D_v + \varepsilon_v + \varepsilon_{sgs} \tag{18}$$

where the different terms can be defined as

mean velocity transfer $T_m = -u_j \langle q^2 \rangle_{,j}$

production $P = -\langle u_i'' u_j'' \rangle u_{i,j}$

turbulent transport $T_t = -\langle u_j'' q_j^2 \rangle$

transport by SGS stresses $T_{sgs} = -\langle u_i'' \tau_{ij} \rangle_{,j}$

buoyancy sink $\beta = \beta g \langle u_i'' T'' \rangle$

pression diffusion $D_p = -\frac{1}{\rho} \langle u_i'' p'' \rangle_{,i}$

viscous diffusion $D_v = \nu \langle q^2 \rangle_{,jj}$

viscous dissipation $\varepsilon_v = -\nu \langle u_{i,j}'' u_{i,j}'' \rangle$

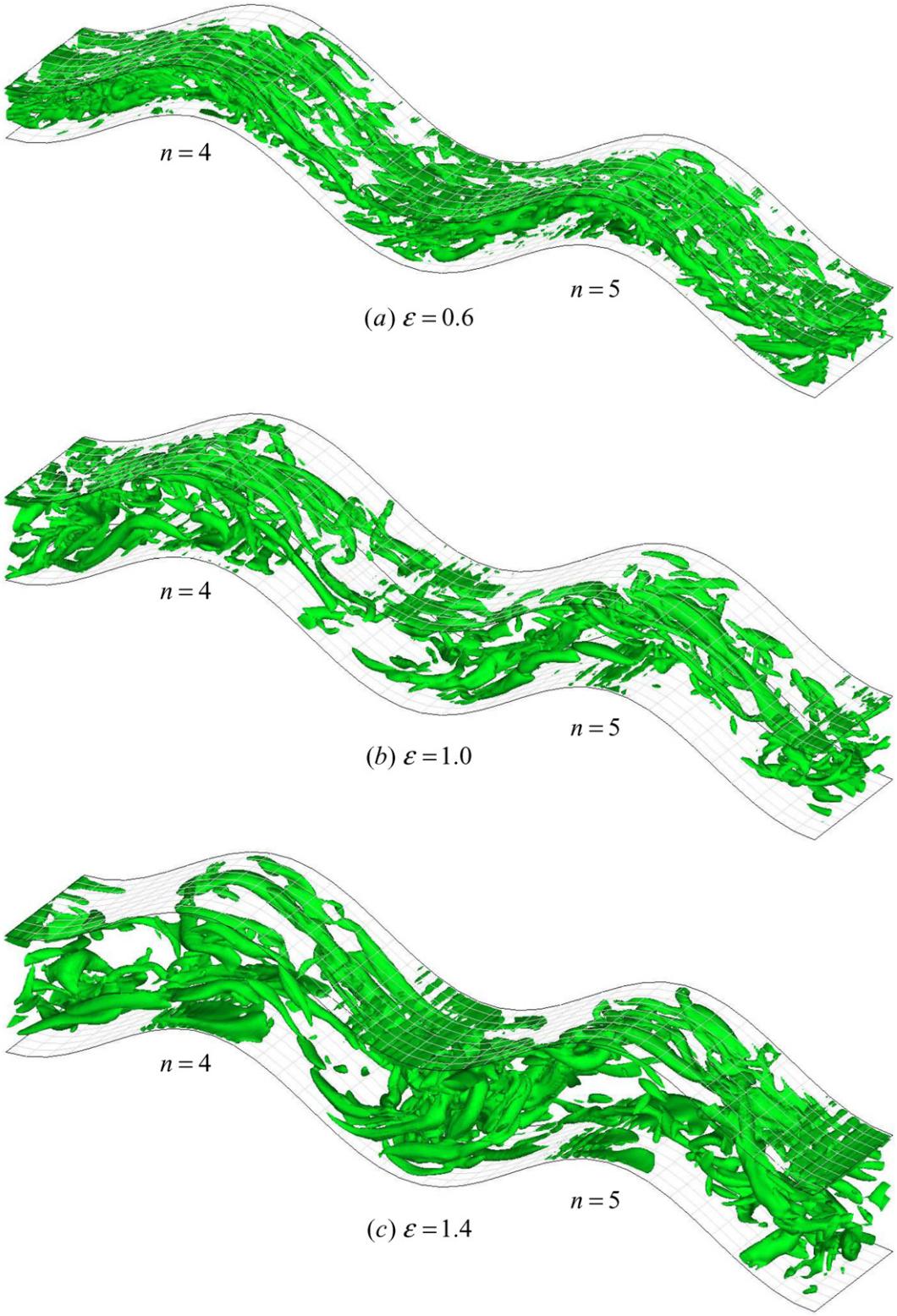

Fig. 10. 3D iso-surface distribution of λ_{ci}^2 for $Re = 3000$ with regard to ε spacing ratios along wavy periods 4 and 5.

SGS dissipation $\varepsilon_{sgs} = \langle u''_{i,j}\tau''_{ij}\rangle$

From Eq. (18), the balance of TKE requires nine different terms but it was found that only four of them were significant in the equation: T_m mean transport term, P production, T_t turbulent transport and ε_v viscous dissipation terms are the most dominant terms and their spatial distribution alone is plotted in Fig. 11 for two different spacing ratio ($\varepsilon = 0.6$ and 1.4).

Since the gradients of TKE are strong in the vertical direction, the second term of Eq. (18) is significant. For $\varepsilon = 1.4$, i.e. when the two wavy channels are the most markedly separated, a region with strong production of TKE develops from the crest of the lower wall and in its wake, this mainly occurs in the trough (crest) of the

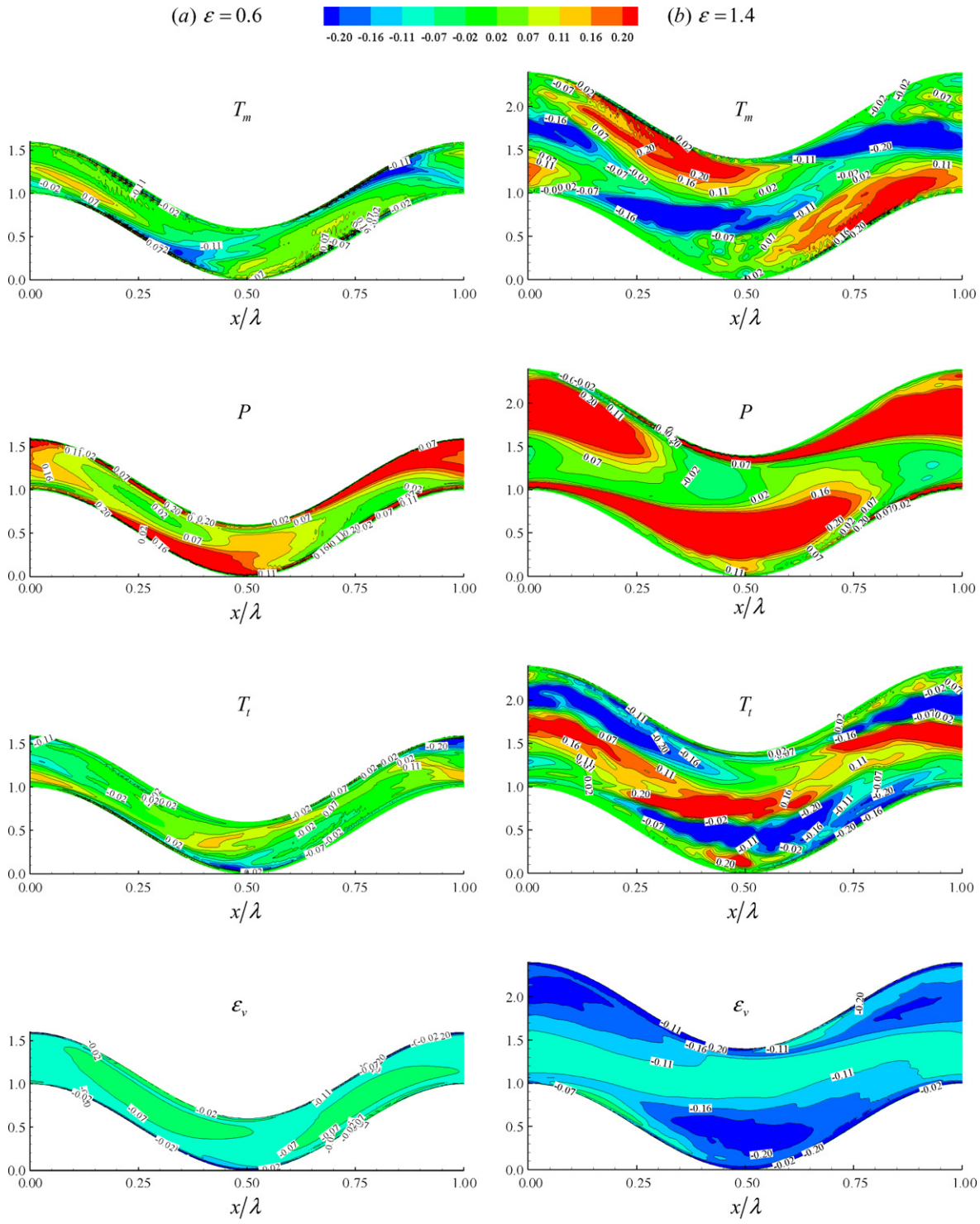

Fig. 11. Contours of the four main components (T_m, P, T_t, ε_v) of TKE budget along wavy period 5 for $\varepsilon = 0.6$ and 1.4.

lower (upper) wall. That said, the production region is analogously reported by Calhoun and Street (2001) in their analysis of flow over a wavy surface. As regards of a wavy channel, production mainly occurs in the trough and does not undergo much vertical expansion; this is due to the main flow, which is deviated by the upper wavy wall presence. When the latter is located quite close to the lower one ($\varepsilon = 0.6$), production does not occur in the wake of crests or troughs but is mainly confined to the down-slope (up-slope) along the lower (upper) wall. TKE is generated mainly along the wavy walls while gradients in the main part of the channel are reduced except close to the walls by the decrease of ε. T_m transport of TKE is also pronouncedly affected by the ε spacing ratio. For $\varepsilon = 0.6$, T_m negative regions are observed along the down-slope (up-slope) lower (upper) wavy walls, which indicates that mean velocity transport would tend to decrease TKE. As underlined by Calhoun and Street, the physical meaning of the sign of T_m is that where T_m is negative, the mean velocity field tends to bring in fluid with a lower TKE; where T_m is positive, the mean field brings in high-TKE fluid. Note that in the case of $\varepsilon = 1.4$, negative T_m region is located in the wake of crests (troughs) for the lower (upper) wavy

walls, while positive T_m regions mainly arise in the vicinity of wavy walls. As concerns T_t turbulent transport of TKE, a central layer of strong negative transport is bordered above and below by weaker regions of positive transport in the trough for $0.25 \leqslant x/\lambda \leqslant 0.75$ and even if these distributions are confined to the trough and do not expand vertically, similar behaviour in the T_t turbulent transport was underlined in flow over a wavy surface. Once again, the spatial distribution of T_t turbulent transport for $\varepsilon = 0.6$ is significantly modified, which is also the case with ε_v viscous dissipation. The latter is naturally negative over the whole domain but gradients of ε_v are weak for $\varepsilon = 0.6$ while stronger dissipative regions can easily be distinguished either in the trough (crest) for lower (upper) wavy wall. From the TKE balance, the effect of ε spacing ratio is clearly highlighted. As soon as ε is great enough, flow field is forced to be sheared continuously in the wake of crest and troughs emphasizing large coherent structures and turbulence production. It consequently favours also convection transport, and turbulent dissipation as well as viscous dissipation. For a smaller spacing ratio ($\varepsilon = 0.6$), flow nature is also fully turbulent but shear is produced mainly from the non-slip wall condition and wake unsteadiness are reduced. As a result, the main components of TKE balance are more homogeneously distributed along the wavy period. The way turbulence behaves is then strongly affected by the ε spacing ratio. In order to shed light on the effect of ε along one wavy period, τ_w surface shear stress and the *Nu* Nusselt number along one wavy period are plotted in Fig. 12 for several ε levels along the lower wall of wavy period 5 where flow is fully developed and turbulent. For $\varepsilon = 1.4$, a maximum peak of τ_w is detected upstream of the crest, which corresponds to flow reattachment on both sides of the crest while for $0.1 \leqslant x/\lambda \leqslant 0.6$, τ_w values are negatives illustrating the separation of the flow field along the downslope wavy wall. Heat transfer is thereby strongly reduced in that region, with levels lower than 0.01, while for $x/\lambda \geqslant 0.6$, a plateau is reached at a maximum level of *Nu* at 0.04. As soon as ε is reduced and under the same *Re* Reynolds number (*Re* = 3000), the changes of both τ_w and *Nu* are reduced. For instance a maximum level of τ_w is about 0.04 for $\varepsilon = 1.4$ while it does not exceed 0.025 for $\varepsilon = 0.6$; at the same time, minima of τ_w are approximately 0.0 and 0.01 for $\varepsilon = 1.0$ and 0.6, respectively. ε spacing ratio has thus great influence on both τ_w and *Nu* by rendering their spatial distribution more homogeneous as well. In the *Nu* distribution, while a plateau at $Nu \sim 0.03$ still occurs in the up-slope ($x/\lambda \geqslant 0.6$) for $\varepsilon = 1.0$, only a peak of about $Nu = 0.026$ approximately arises at $x/\lambda \sim 0.55$. Finally, in order to estimate the overall performance of heat and mass transfer, we have computed the *f* Fanning factor and *j* Colburn coefficient as well as *j*/*f* efficiency factor and their modifications with regard to ε are plotted in Fig. 13. As expected, the

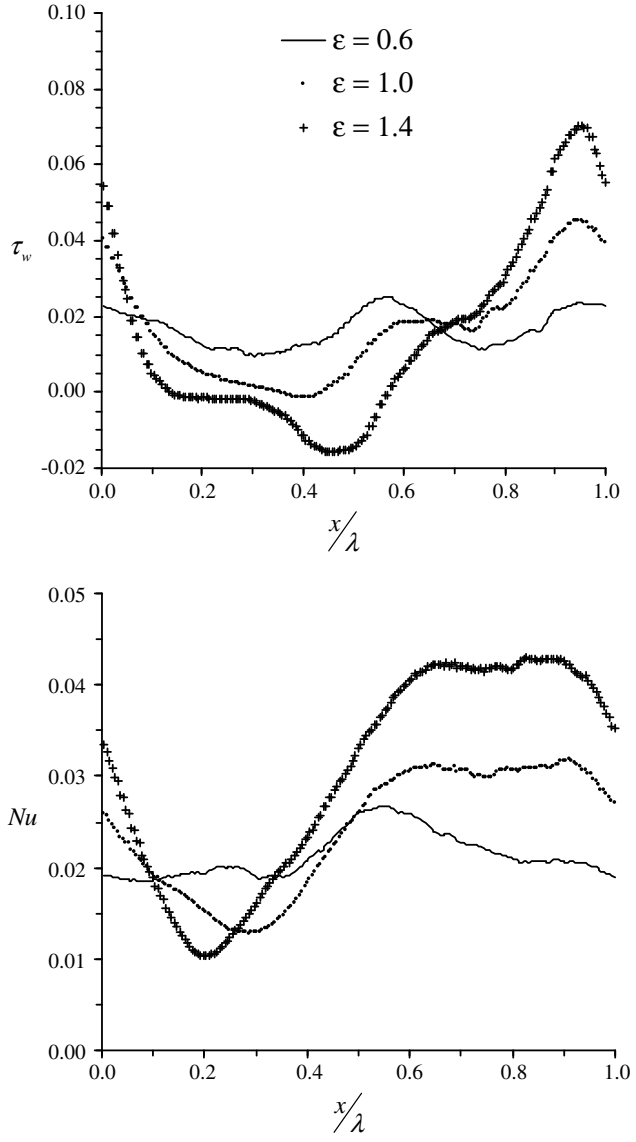

Fig. 12. Time-averaged surface shear stress τ_w and Nusselt number *Nu* with regard to ε along wavy period 5.

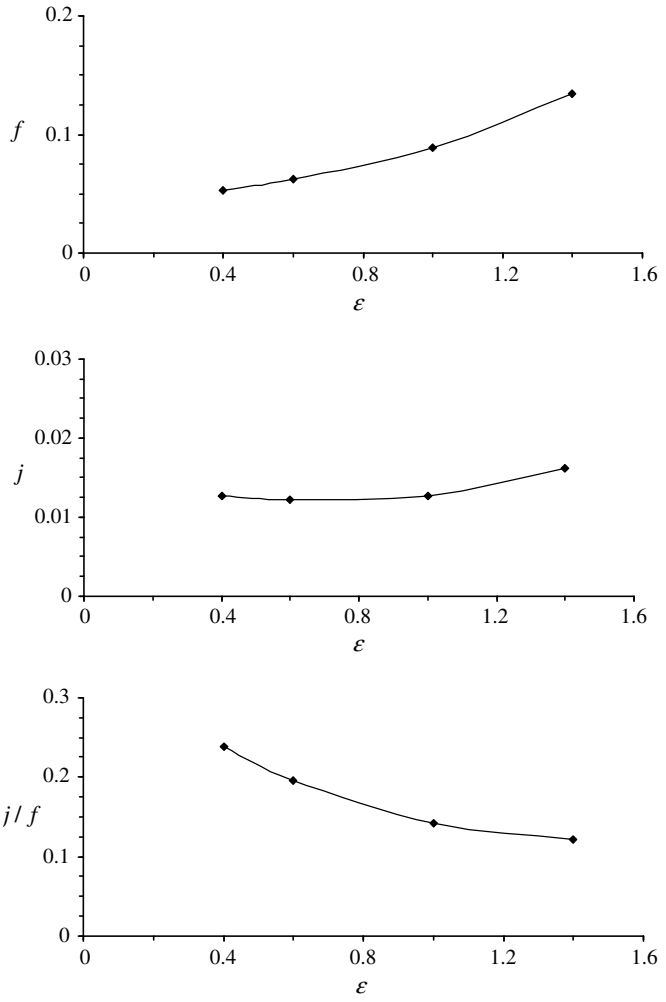

Fig. 13. Global variations of *j* heat transfer coefficient, *f* friction factor and *j*/*f* ratio versus *Re* Reynolds numbers with regard to ε.

greater ε the stronger f. This is due to the fact that large ε configuration favours shear-layer development in the wake of crests and troughs that significantly contributes to friction enhancement. In fact f is amplified by a factor of 2.2 from $\varepsilon = 0.4$ and 1.4 while at the same time, heat transfer is not amplified quite as much. Although larger ε favours significant spatial variations in Nu, the average Nu or j remains at an almost constant level or at least is slightly increased. As a result, the j/f ratio asymptotically decreases with regard to ε varying from almost 0.25 to 0.125 from $\varepsilon = 0.4$ to 1.4.

4. Conclusion

Large-eddy simulation was employed to address a major point in heat transfer by studying fluid flow behaviour in sinusoidal wavy channels for a wide range of Reynolds number levels, i.e. from 750 up to 4500. No periodic conditions in the streamwise direction were applied so as to capture the different flow field regions. Regarding the Re Reynolds levels, a wavy channel characterized by ε spacing ratio and γ waviness aspect ratio of 1.0 and 0.2, respectively, was more specifically analyzed and with a vortex structure identification method, it became possible to shed light on the different flow field behaviors. First and as expected, the unsteadiness of the flow occurs sooner spatially for large Re levels while in the whole computational domain, a strong unsteadiness occurs but no turbulent regime is detected for $Re \leqslant 1500$. On the contrary, for higher Re levels the flow turns to turbulence from wavy period 4. The influence of the ε spacing ratio was studied in order to depict its role in the turbulent development of wavy channel flows; three different ε spacing ratio levels were analyzed for $Re = 3000$. It was clearly shown that the smaller ε the greater the flow in the streamwise direction. Results also shed light on the role of the top wavy wall, which clearly interacts in the turbulence process. The confinement imposed by the presence of the top wavy wall reduces breakdown of structures created along up-slopes (down-slope) along the lower (upper) wavy wall. The specific vortex shapes are then strongly linked to ε. From the balance of turbulent kinetic energy, it was shown that the spacing ratio controls the production regions of TKE mainly by limiting gradients in the trough and crest wakes.

Overall heat and mass transfer was also estimated either with regard to the influence of ε and Re. In order to propose a validation process for our numerical investigation, we simulated an available experimental set-up and our data were found to fit fairly well with the experimental data. We computed the f Fanning factor and j Colburn coefficient and differences were found to be smaller than 4% and 14% for j and f, respectively. By defining overall transfer efficiency from the j/f ratio, the smaller ε the better j/f. In fact, while heat transfer is not significantly improved by a change of ε, f friction is found to be highly sensitive to ε; this is due to the fact that friction arising from shear-layers is limited for smaller ε ratios. Finally, even if the results need to be confronted with numerical issues, namely an extension to the computational domain to expand the scope of our analysis, j/f best rates were found in unsteady flow regimes that occur prior to any transition to turbulence. One way to significantly improve the overall heat and mass transfer would consist on maintaining such unsteady regime as long as possible and that is surely a key point needing to be addressed in the near future.

References

Balaras, E., 2004. Modelling complex boundaries using an external force field on fixed Cartesian grids in large-eddy simulations. Comput. Fluid 33, 375–404.

Blancher, S., Creff, R., Le Quéré, P., 2004. Analysis of convective hydrodynamic instabilities in a symmetric wavy channel. Phys. Fluids 16 (10), 3726–3737.

Blancher, S., Creff, R., Le Quéré, P., 1998. Effect of Tollmien Schlichting on wave convective heat transfer in a wavy channel. Part 1: Linear analysis. Int. J. Heat Fluid Flow 19, 39–48.

Calhoun, R.J., Street, R.L., 2001. Turbulent flow over a wavy surface: neutral case. J. Geophys. Res. 106, 9277–9293.

Cherukat, P., Na, Y., Hanratty, T.J., McLaughlin, J.B., 1998. Direct numerical simulation of a fully developed turbulent flow over a wavy surfaces. Theor. Comput. Fluid Dynam. 11, 109–134.

Choi, H.S., Suzuki, K., 2005. Large eddy simulation of turbulent flow and heat transfer with one wavy channel. Int. J. Heat Fluid Flow 26, 681–694.

Chong, M.S., Perry, A.E., Cantwell, B.J., 1990. A general discussion of three-dimensional flow fields. Phys. Fluids A 2, 765–777.

Conway, S., Caraeni, D., Fuchs, L., 2000. Large eddy simulation of the flow through the blades of a swirl generator. Int. J. Heat Fluid Flow 21 (5), 664–673.

De Angelis, V., Lombardi, P., Banerjee, S., 1997. Direct numerical simulation of turbulent flow over a wavy channel. Phys. Fluids 9, 2429–2442.

Fadlun, E.A., Verzicco, R., Orlandi, P., Mohd-Yusof, J., 2000. Combined immersed-boundary finite-difference methods for three-dimensional complex flow simulations. J. Comput. Phys. 161, 35–60.

Germano, M., Piomelli, U., Moin, P., Cabot, W.H., 1991. A dynamic subgrid-scale eddy viscosity model. Phys. Fluids A 3 (7), 1760–1765.

Hanjalic, K., 2004. Will RANS survive LES? A view of perspectives. In: Proceedings of HT-FED04, ASME Heat Transfer/Fluids Engineering Summer Conference, Charlotte, NC, USA, July 11–15.

Henn, D.S., Sykes, R.I., 1999. Large-eddy simulation of flow over wavy surfaces. J. Fluid Mech. 383, 75–112.

Hunt, J.C.R., Wray, A.A.A., Moin, P., 1988. Eddies; stream and convergence zones in turbulent flows. In: Proceedings of the Summer Program of the Center for Turbulence Research, NASA Ames/Stanford University, pp. 193–207.

Kim, J., Moin, P., Moser, R.D., 1987. Turbulent statistics in fully developed channel flow at low Reynolds number. J. Fluid Mech. 177, 133–166.

Lai, M.C., Peskin, C.S., 2000. An immersed boundary method with formal second-order accuracy and reduced numerical viscosity. J. Comput. Phys. 160, 705–719.

Manglik, R.M., Zhang, J., Muley, A., 2005. Low Reynolds number forced convection in three-dimensional wavy-plate-fin compact channels: fin density effect. Int. J. Heat Mass Transfer 48, 1439–1449.

Najm, H.N., Wyckoff, P.S., Knio, O.M., 1998. A semi-implicit numerical scheme for reacting flow. J. Comput. Phys. 143, 381–402.

Niceno, B., Nobile, E., 2001. Numerical analysis of fluid flow and heat transfer in periodic wavy channels. Int. J. Heat Fluid Flow 22, 156–167.

Nishimura, T., Matsume, S., 1998. Vortices and shear stresses in asymmetric and symmetric channels with sinusoidal wavy walls for pulsatile flow at low Reynolds numbers. Int. J. Heat Fluid Flow 19, 583–593.

Peskin, C.S., 1972. Flow patterns around heart valves: a numerical method. J. Comput. Phys. 10, 252–271.

Peskin, C.S., 1977. Numerical analysis of blood flow in the heart. J. Comput. Phys. 25, 220–252.

Pham, M.V., Plourde, F., Doan Kim, S., 2003. LES simulation in a thin liquid film submitted to high thermal stress. In: ASME Summer Heat Transfer Conference, Las Vegas, July 21–23.

Pham, M.V., Plourde, F., Doan, K.S., Balachandar, S., 2006. Large-eddy simulation of a pure thermal plume under rotating conditions. Phys. Fluids 18, 1–14.

Pham, M.V., Plourde, F., Doan Kim, S., 2007. Strip decomposition parallelization of fast direct Poisson solver on a 3D Cartesian staggered grid. Int. J. Comput. Sci. Eng. 1, 31–40.

Pham, M.V., Plourde, F., Doan Kim, S., 2008. Large-eddy simulation of staggered parallel-plate fin heat exchangers – effects of Reynolds number on flow topology. Numer. Heat Transfer J. 53, 354–376.

Rush, T.A., Newell, T.A., Jacobi, A.M., 1999. An experimental study of flow and heat transfer in sinusoidal wavy passages. Int. J. Heat Mass Transfer 42, 1541–1553.

Saric, W.S., Benmalek, A., 1991. Görtler vortices with periodic curvature. Boundary layer stability and transition to turbulence. ASME FED 114, 37–42.

Tafti, D.K., Wang, G., Lin, W., 2000. Flow transition in a multilouvered fin array. Int. J. Heat Mass Transfer 43, 901–919.

Tseng, Y.H., Ferziger, J.H., 2003. A ghost-cell immersed boundary method for flow in complex geometry. J. Comput. Phys. 192, 593–623.

Tseng, Y.H., Ferziger, J.H., 2004. Large-eddy simulation of turbulent wavy boundary flow—illustration of vortex dynamics. J. Turb. 5 (34), 1–23.

Udaykumar, H.S., Mittal, R., Rampunggoon, P., Khanna, A., 2001. A sharp interface Cartesian grid method for simulating flows with complex moving boundaries. J. Comput. Phys. 174, 345–380.

Yang, J., Balaras, E., 2006. An embedded-boundary formulation for large-eddy simulation of turbulent flows interacting with moving boundaries. J. Comput. Phys. 215, 12–40.

Zang, Y., Street, R.L., Koseff, J.R., 1993. A dynamic mixed subgrid-scale model and its application to turbulent recirculating flows. Phys. Fluids A 5, 3186–3196.

Zhang, J., Muley, A., Borghese, J.B., Manglik, R.M., 2003. Computational and experimental study of enhanced laminar flow heat transfer in three-dimensional sinusoidal wavy-plate-fin channels. In: ASME Summer Heat Transfer Conference, Las Vegas, NV, July 21–23.

Zhang, J., Kundu, J., Manglik, R.M., 2004. Effect of fin waviness and spacing on the lateral vortex structure and laminar heat transfer in wavy-plate-fin cores. Int. J. Heat Mass Transfer 47, 1719–1730.

Zhang, W., Chen, Q., 2000. Large eddy simulation of natural and mixed convection airflow indoors with two simple filtered dynamic subgrid scale models. Numer. Heat Transfer Pt. A 37, 436–447.